

POLITECNICO DI TORINO

Master Degree in Mechatronic Engineering

Master Thesis

**Analysis of thermal propagation  
behaviour of Li-ion cells under various  
boundary conditions considering  
breathing and swelling mechanisms**



**Politecnico  
di Torino**

**Supervisors**

Prof. Silvia BODOARDO

Prof. Alessandro RIZZO

**Candidate**

Annalisa COPPOLA

ID: 263640

**Internship Supervisor**

**TU Graz, Vehicle Safety Institute (Graz, Austria)**

Dipl.-Ing. Simon Franz HEINDL

**ACADEMIC YEAR 2020-2021**

*To my granny*

# Abstract

In the literature, various methods have been shown for analyzing thermal parameters. However, the disadvantage of these methods is that they do not consider how the volume change due to breathing and swelling phenomena during the charging and discharging cycles can affect the thermal parameters. To this end, the purpose of the thesis is divided into two parts. The first part deals with a thermal characterization through a software simulation, COMSOL Multiphysics, of the lithium-ion cells with an existing device. On the other hand, the idea is to measure the heat flux inside the battery by applying different pretension force values to different battery temperature values in order to recreate the different cell volume changes, understand how the geometry of the battery is connected to the thermal parameters, how these parameters change according to an external mechanical force applied and even try to understand if it is possible to counteract the swelling phenomenon and therefore the degradation of the cell itself thanks to external pressure. Furthermore, since the current device considered is composed of several sensors, including the one considered in this case, the heat flux sensor, it is advisable to understand what the maximum load it can withstand is. Hence, it is possible to introduce the second part on which the thesis is focused: applying an external pretension force with a range of [0-20k]N, how a heat-flux sensor can react, what is the maximum applicable force value that the sensor can withstand before breaking, and if changing different values of force and temperature, the sensor output is always the same or can vary. Therefore, the second part aims to analyze and simulate via software the behavior of the heat flux sensor *FHF02*, creating a suitable structure. The structure is composed of a heat source, a cooling system, and an external device that gradually applies at different  $\Delta T$ , increasing force values up to the limit of the sensor itself. Thus, this research provides a simulated basis for future experiments in real life to understand how to study the thermal behavior of the battery concerning mechanical behavior without destroying all the devices involved in the experiment.

# Vehicle Safety Institute - TU Graz

This Master's Thesis is a collaboration between the Politecnico di Torino University and VSI (Vehicle Safety Institute), a research center at Graz University of Technology, focuses on safety of vehicles with different levels of automation, safety of alternatively powered vehicle concepts and development of methods for the evaluation of systems to prevent accidents and reduce injuries. Therefore, basic research in the interdisciplinary fields of "Safety Aspects of Electric Energy Storage Systems", "Critical Traffic Scenarios", "Human Modeling with focus on Trauma Biomechanics" and "Crashworthiness of (Bio)Materials" is carried out.[1]



Figure 1: Vehicle Safety Institute logo [1]

# Contents

Vehicle Safety Institute - TU Graz . . . . .	4
<b>List of Figures</b>	<b>7</b>
<b>List of Tables</b>	<b>10</b>
<b>1 Introduction</b>	<b>11</b>
1.1 Field of work . . . . .	11
1.2 Problem description . . . . .	11
1.2.1 Breathing and swelling mechanisms . . . . .	11
1.2.2 Impact of breathing and swelling on lithium-ion battery	16
1.2.3 Research question . . . . .	18
1.2.4 Thesis outline . . . . .	19
<b>2 State of the art</b>	<b>21</b>
2.1 Theory . . . . .	21
2.1.1 Definition of thermal parameters . . . . .	23
2.2 Thermal characterization of the cell: review of literature . . .	25
2.2.1 I experiment [2] . . . . .	25
2.2.2 II experiment [3] . . . . .	28
2.2.3 III experiment[4] . . . . .	31
2.2.4 IV experiment[5] . . . . .	33
2.2.5 V experiment [6] . . . . .	35
2.2.6 Comparison between the methods . . . . .	37
<b>3 Heat flux sensor</b>	<b>39</b>
3.1 Working principle of the heat flux sensor . . . . .	39
3.1.1 Calibration . . . . .	41

<b>4</b>	<b>Modeling &amp; Simulation</b>	<b>43</b>
4.1	Experiment with existing device . . . . .	43
4.1.1	Simulation of the experiment . . . . .	47
4.1.2	Results . . . . .	52
4.2	Modelling and simulation of a new device . . . . .	66
4.2.1	Method . . . . .	67
4.2.2	Experiment design . . . . .	69
4.2.3	Heating Source . . . . .	71
4.2.4	Cooling device . . . . .	74
4.2.5	Mechanical properties of the structure . . . . .	75
4.2.6	Energy balance . . . . .	80
4.2.7	Heat source . . . . .	83
<b>5</b>	<b>Conclusion &amp; Outlook</b>	<b>89</b>
	<b>Bibliography</b>	<b>91</b>

# List of Figures

1	Vehicle Safety Institute logo [1]	4
1.1	Structure of a lithium-ion battery [7]	12
1.2	Charging phase [7]	13
1.3	Discharging phase [7]	13
1.4	Mechanism of Deep Discharge in a Lithium-Ion Battery [8]	15
1.5	CT scan of battery from deep discharge swelling [8]	16
2.1	Graph Temperature-Power Limits of LIB[9]	23
2.2	Structure of Li-ion pouch cell[10][11]	25
2.3	Cross-sectional view of the developed THFS unit with its corresponding equivalent circuit model (ECM) as used for the one-dimensional thermal analysis[2]	26
2.4	Measured heat flux density for a cell after 60 min cycling loading with 2C-rate and actively controlled surface temperature of 25°C[2]	27
2.5	Measured temperature distribution of the prismatic battery cell with a constant temperature of 25°C on the bottom side and continuous 2C loading[2]	28
2.6	Experimental set-up for thermal impedance measurement on cylindrical battery using external heating coil for generating heat pulse[3]	29
2.7	Setup[4]	32
2.8	Schematic of the isothermal calorimeter[5]	34
2.9	Through-plane thermal conductivity of the cell as a function of temperature for different SoC levels[5]	35
2.10	Test setup[6]	36
3.1	General working principle of heat flux sensor[12]	40
3.2	Ideal curve of a sensor[13]	40

3.3	K-type thermocouple (chromel–alumel) in the standard thermocouple measurement configuration.[14] . . . . .	42
4.1	Reference system used for the orientation of the orthotropic thermal conductivity measurements. The “w” vector is on the battery thickness direction, “v” vector is parallel to the tabs direction, and “u” vector is perpendicular to them [15] . . . . .	44
4.2	General assembly of temperature-guarded plate (Peltier plate). The heatsinks were fixed to the aluminum plate with nylon bolts in order to increase the efficiency of the system. Digital temperature sensors DS1820B+ with 0.5 C uncertainty were placed inside the aluminum plate volume. [15] . . . . .	45
4.3	Test bench [15] . . . . .	46
4.4	Schematic diagram showing the expected heat flux for the measurement of the thermal conductivity along the longitudinal directions. [15] . . . . .	47
4.5	Schematic of a 3D single-layer cell [16] . . . . .	48
4.6	Simulated 3D single-layer pouch cell . . . . .	48
4.7	Simulated test bench in "w" direction (top view) . . . . .	49
4.8	Simulated test bench (side view) . . . . .	49
4.9	Simulated test bench in longitudinal directions . . . . .	49
4.10	Simulated test bench in longitudinal directions (side view) . . . . .	50
4.11	Schematic of a Peltier cell [17] . . . . .	50
4.12	Peltier cell (external view) . . . . .	50
4.13	Peltier cell (internal view) . . . . .	51
4.14	Surface temperature Peltier . . . . .	51
4.15	Drawing of the heating circuit deposited on a glass plate [18] . . . . .	52
4.16	Mat heater [18] . . . . .	52
4.17	Experimental plots relative to sample 2 in "w" direction [15] . . . . .	53
4.18	Simulated plots relative to sample 2 in "w" direction . . . . .	54
4.19	Experimental plots relative to sample 3 in "w" direction [15] . . . . .	55
4.20	Simulated plots relative to sample 3 in "w" direction . . . . .	56
4.21	Experimental plots relative to sample 2 in "v" direction [15] . . . . .	57
4.22	Simulated plots relative to sample 2 in "v" direction . . . . .	58
4.23	Experimental plots relative to sample 3 in "v" direction [15] . . . . .	59
4.24	Simulated plots relative to sample 3 in "v" direction . . . . .	60
4.25	Experimental plots relative to sample 2 in "u" direction [15] . . . . .	61
4.26	Simulated plots relative to sample 2 in "u" direction . . . . .	62
4.27	Experimental plots relative to sample 3 in "u" direction [15] . . . . .	63

4.28	Simulated plots relative to sample 3 in "u" direction . . . . .	64
4.29	3D Multilayer cell [16] . . . . .	65
4.30	FHF02 sensor [12] . . . . .	66
4.31	Schematic FHF02 sensor [12] . . . . .	67
4.32	Flowchart of a possible method to study the heat flux sensor behavior . . . . .	68
4.33	Complete structure . . . . .	71
4.34	Complete structure from different views . . . . .	71
4.35	Aluminum block of the upper part and holes dimensions . . . . .	72
4.36	Aluminum block of the upper part and holes dimensions (top view) . . . . .	72
4.37	Complete model of heat source with heat flux sensor . . . . .	73
4.38	heat source front view [19] . . . . .	74
4.39	Complete model of cooling device . . . . .	74
4.40	Cooling device (top view) . . . . .	75
4.41	Cooling device measurements . . . . .	75
4.42	Mechanical study of heat source (stress) . . . . .	76
4.43	Mechanical study of heat source (elongation) . . . . .	77
4.44	Schematic of the lower part (1) . . . . .	78
4.45	Schematic of the lower part (2) . . . . .	79
4.46	Mechanical study of cooling device (stress) with first dimensions . . . . .	79
4.47	Mechanical study of cooling device with second dimensions . . . . .	80
4.48	Equivalent electrical scheme . . . . .	81
4.49	Temperature profile . . . . .	82
4.50	Calibration: Temperature study . . . . .	83
4.51	$Q_{needed}$ from 0 to 5 min . . . . .	84
4.52	Heating at different minutes . . . . .	85
4.53	Heat source with EPS box . . . . .	86
4.54	Heat source with EPS box: temperature study . . . . .	87
4.55	$Q_{loss}$ with EPS box from 0 to 5 min . . . . .	87

# List of Tables

2.1	Temperature range for different battery types [20] . . . . .	22
2.2	Average heat flux density on the different sides of the battery cell at $t = 60$ min [2] . . . . .	28
2.3	Heat transfer coefficients, specific heat and thermal conductivity of cylindrical Li-ion batteries [3] . . . . .	30
2.4	In-plane and cross-plane thermal properties of Sony US-18650 lithium-ion battery components with and without electrolyte [4] . . . . .	33
2.5	Thermal parameters of the Li-ion pouch cell[6] . . . . .	37
2.6	Comparison between thermal characterization methods . . . . .	37
4.1	Thicknesses of Single Layer Component Samples, Prepared by the BIB-Cutting Method [21] . . . . .	45
4.2	Experimental and simulated measurements in "w" direction - Sample 2 and 3 . . . . .	53
4.3	Experimental and simulated measurements in "v" direction - Sample 2 and 3 . . . . .	53
4.4	Experimental and simulated measurements in "u" direction - Sample 2 and 3 . . . . .	53
4.5	FHF02 Specifications [12] . . . . .	67

# Chapter 1

## Introduction

### 1.1 Field of work

Rechargeable batteries are the most widely used energy storage systems in the consumer electronics industry today and the most promising technology for sustainable electric transportation.

Lithium-ion batteries are currently used in various sectors, including consumer electronics such as cell phones, computers, tablets, and industrial, medical, and household applications.

Moreover, they represent an essential technology for integrating renewable sources, which, being intermittent and not easy to manage, require efficient storage systems to ensure numerous charge-discharge cycles, high conversion efficiencies, and low physical degradation over time.

In this regard, it is essential to note that during the charging and discharging of Li-ion batteries, the volume of the cell changes reversibly due to intercalation (“breathing”) and not-reversibly due to aging effects (“swelling”).

For this reason, the object of the thesis is how the breathing and swelling mechanisms and their consequences can affect the thermal parameters of a Li-ion battery cell.

### 1.2 Problem description

#### 1.2.1 Breathing and swelling mechanisms

The battery is an electrochemical device capable of storing electrical charge and returning it in the discharge phase. The basic unit of a battery is the

cell, which creates the module when joined in series or parallel with other identical cells. The combination of several modules creates the battery pack. Lithium cells consist of a negative electrode (anode) and a positive electrode (cathode), immersed in an electrolyte usually consisting of lithium salts dissolved in organic solvents and a polymer membrane as a separator that prevents the passage of electrons, but is nevertheless permeable to the passage of ions (1.1). The anode is made of carbon, and, in general, graphite is used. The cathode is made from metal oxides and, among the many possible compositions, can be lithium cobalt oxide ( $LiCoO_2$ ), lithium iron phosphate ( $LiFePO_4$ ) or lithium manganese oxide ( $LiMnO_4$ ). Of these,  $LiCoO_2$  is a good solution for high capacity and maturity in the creation process. It has, however, one major limitation since it is very toxic; the material is expensive and has low thermal stability. For all these reasons, there is a tendency to use  $LiFePO_4$  as they are safer and more thermally stable. The electrolyte is an electronically insulating but ionically conductive medium. It transports the reactant between the two electrodes without short-circuiting the battery. It is made from a lithium salt dissolved in an organic solvent such as ethylene carbonate (EC), diethyl carbonate (DEC), propylene carbonate (PC), or dimethyl carbonate (EMC). The current collectors are made of copper (Cu) for the negative electrode and aluminum (Al) for the positive one.[22]

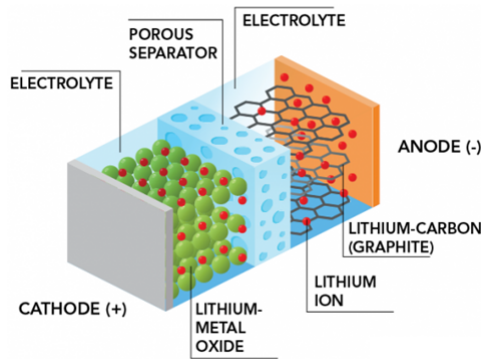


Figure 1.1: Structure of a lithium-ion battery [7]

The working principle of lithium-ion cells is not influenced by the design, geometry, or materials used but is based on the **intercalation** phenomenon. The charging and discharging processes are associated with redox reactions that result in the migration of lithium ions from one electrode to another. During the charging process, positive lithium ions ( $Li^+$ ) are extracted from the cathode and transferred to the anode through the electrolyte and, to keep the electric equilibrium, the same number of electrons migrate from

the cathode to the anode through the external circuit that powers the cell, resulting in oxidation of the cathode. The lithium ions are thus intercalated in the graphite matrix of the anode and are reduced to lithium, acquiring electrons from the cathode through the external circuit (1.2).

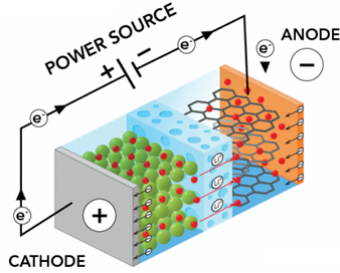


Figure 1.2: Charging phase [7]

Dually, during the discharging process of the cell, the lithium atoms present in the anode release electrons, which are transferred to the cathode via the external circuit, while the positive lithium ions ( $Li^+$ ) migrate, through the electrolyte, to the cathode where the reduction of the latter takes place (1.3). During the process of an electrochemical cell, including lithium cells, charged particles, whether ions or electrons are transferred from the cathode to the anode and vice versa, depending on whether energy is being stored or supplied.[23]

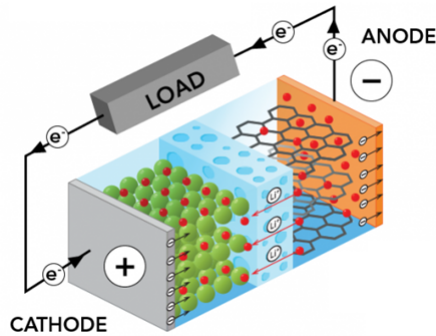
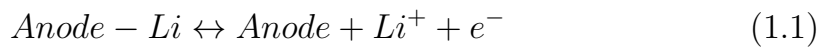


Figure 1.3: Discharging phase [7]

The overall cell reaction is shown in equations (1.1) (anodic) and (1.2) (cathodic), where left to right denotes the discharge of cell and vice versa.[24]





Interestingly, the intercalation and deintercalation of Li ions in the graphite particles induced by charging and discharging lead to expansion and contraction of the layered materials; hence, it is possible to observe the battery volume changes. This consequence is a reversible process and is called **breathing**. The insertion and extraction of lithium ions result in expansion and contraction, respectively. For instance, the distance between graphite layers increases by 10% due to intercalation. The volume changes correspond to the amount of Li-ion insertion or extraction.[25]

A team of researchers at MIT (Massachusetts Institute of Technology), the University of Southern Denmark, Rice University, and Argonne National Laboratory has determined that the electrode materials are generally crystalline, with all their atoms neatly arrange in a regular, repetitive array, when they undergo the charging or discharging process, they are transformed into a disordered, glass-like phase (amorphous phase), instead of maintaining their precisely ordered lattice, that can accommodate the strain of the dimensional changes.[26]

It must be noted that there are side reactions happening between the electrodes and the electrolyte during several charge-discharge cycling processes, causing some aging mechanisms:

- Many authors and Peled proposed a concept now universally accepted of a Solid Electrolyte Interface (**SEI**), through which lithium ions can move, but preventing the electrons from reaching the molecules species of electrolyte susceptible of reduction. Any defect in the layer protection will result in lithium corrosion, and irreversible energy loss. Because of the high surface area of the porous negative electrode, this feature is more critical in Li-ion batteries, and it a possible source of aging. The continuous change in volume caused by the insertion and extraction of lithium from the anode (graphite) is particularly marked during a deep discharge; the succession of these changes damages the crystal structure, which can eventually crumble. More commonly, micro-fractures are created in which the electrolyte solution is inserted. This means that the protective passivation layer on the anode (SEI) decomposes, with the new electrode and electrolyte surfaces coming in contact, and a new SEI layer is formed, which thickens to the detriment of the active material

(1.4). As a result, there is a decrease in capacitance and an increase in resistance at the interface.[27]

- Lithium-ion batteries use a chemical reaction to generate power. As the battery ages, this chemical reaction no longer completes perfectly; it leads to the creation of a gas (**degassing**) which leads to the battery swelling. In addition, if the overlapping layers of chemicals inside the battery do not maintain adequate separation (due to damage or defects), swelling and even a fire may occur.
- Moreover, the abuse of rapid recharges does not help to the battery life: lithium has much more difficulty in dissolving in the electrolyte, favoring the formation of dendrites and increasing the probability of short circuits. The battery begins to swell both when the chemical reactions do not complete properly (a gas is generated that tends to increase the volume) and when the separation between the electrodes is no longer adequate. In the most compromised situations, humidity in the air can help to accelerate the swelling and degassing process, especially if the separation membrane is damaged.
- Finally, the species produced by cathodic degradation can migrate to the anode and react there, forming other undesirable compounds, including gases.

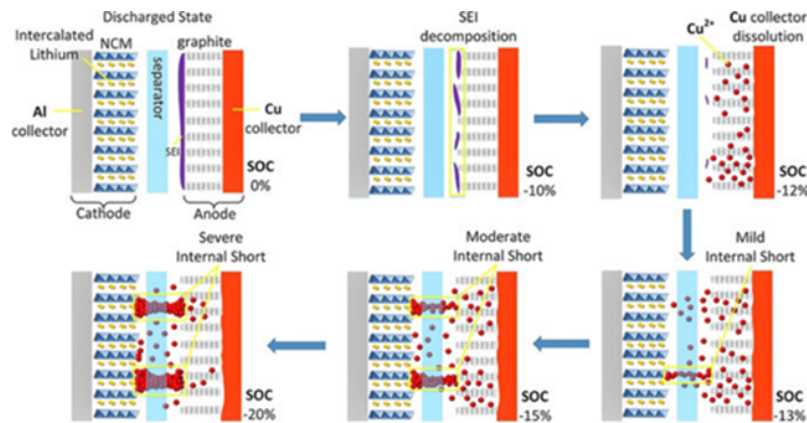


Figure 1.4: Mechanism of Deep Discharge in a Lithium-Ion Battery [8]

Therefore, the main consequence of all the different aging mechanisms previously described is the **swelling** (1.5). The swelling is the effect of particles

that become trapped between the battery layers and end up piercing the membrane separating the layers. If the membrane has been compromised, moisture in the air can react with the cell and cause it to swell. It is caused by orthotropic expansion; hence it occurs mainly in a direction perpendicular to the electrodes, which leads to an increase in the thickness of the cell.

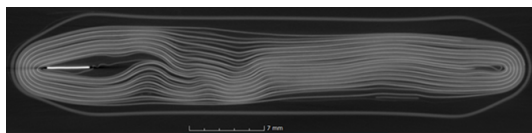


Figure 1.5: CT scan of battery from deep discharge swelling [8]

### 1.2.2 Impact of breathing and swelling on lithium-ion battery

Given what has been previously written, during charging and discharging of Li-ion batteries, the thickness of the cell increases reversibly due to intercalation ("breathing") and not-reversibly due to aging effects ("swelling"). Hence breathing and swelling mechanisms may impact the battery module: indeed, as previously described, swelling can influence the battery's lifetime because if in a battery there is a succession of changes in volume, this can damage the crystalline structure. Also, if the SEI is perforated, it leads to gas formation. Consequently, the copper current collector on the negative electrode starts to dissolve. Upon recharge, these copper ions deposit on electrode or separator surfaces, potentially leading to a copper short and the risk of **thermal runaway**. This phenomenon occurs when a cell, or area within the cell, achieves elevated temperatures due to thermal failure, mechanical failure (which is the case of the breathing and swelling mechanisms), internal/external short-circuiting, and electrochemical abuse. At elevated temperatures, exothermic decomposition of the cell materials begins. Eventually, the self-heating rate of the cell is greater than the rate at which heat can be dissipated to the surroundings, the cell temperature rises exponentially, and stability is ultimately lost. The loss in stability results in all remaining thermal and electrochemical energy being released to the surroundings.[28] Sometimes, with the thermal runaway event, there could be a fire or even an explosion of the cell.

During the charging and discharging process inside the battery, heat is generated. Heat generation in Li-ion batteries includes two main components: reversible heat and irreversible heat. The reversible heat originates

from the entropy change associated with electrochemical reactions. Thus, it is also known as reaction heat or entropic heat. The irreversible heat is comprised of active polarization heat and ohmic heat. The polarization is the deviation between the cell's open-circuit potential and the operating potential. At the solid-electrolyte interface, there is a resistance to hinder the charge transfer process. The energy needed to overcome the barrier during the lithium intercalation and de-intercalation process is referred to as the active polarization heat. The ohmic heat or Joule heat is the energy loss caused by the transport resistance in solid and electrolyte phases. In general, during high charge/discharge rates, the irreversible Joule heat dominates among the total heat generation, and the reversible heat is small compared to the Joule heat. Therefore, it is crucial to maintain temperature homogeneity in lithium-ion batteries to prevent adverse voltage distributions and differential aging within the cell. The properties of lithium-ion cells, such as impedance and capacity, depend strongly on variables such as operating temperature and State of Charge (SoC).[29] During usage, the performance of lithium-ion batteries degrades, and key characteristics, such as capacity and impedance, worsen due to aging mechanisms, e.g., SEI layer growth. Increased impedance is detrimental as less power can be extracted from the cell, and additional heat is generated. Experiments performed at different ambient temperatures have revealed that the aging rate has a strong temperature dependence.[29]

Operating cells at elevated temperatures ( $>25^{\circ}\text{C}$ ) is known to accelerate SEI film growth on the anode and degradation of the cathode, leading to capacity fade and increased internal impedance, the latter producing more heat and accelerating aging.[29] The increased heat generation may have catastrophic consequences such as thermal runaway if the cell temperature cannot be managed to an appropriate level throughout battery life for a range of different environmental conditions and use cases.[29] Because of thermal gradients, the cell does not age uniformly, and an aging gradient occurs inside the cell, reducing the efficiency and lifespan of lithium-ion batteries.[30]

Another consequence of these phenomena could be the compression of cells. At present, pouch cell is one of the favorite choices by automotive manufactory or battery packs because of its high flexibility in packaging compared with cylindrical and prismatic design formats. Although easily stackable, the swelling phenomenon appears. More miniature packs can inflate about 8-10% over 500 cycles; more giant cells may expand to that size after 5000 cycles. This stress can lead to compression of the cells between

themselves or with their environment, which could influence the performance of lithium-ion pouch cells and lead to safety issues.

Moreover, it can be noticed that the pressure of the battery changes during power cycling. Indeed, it decreases during the discharge phase and increases during the charge phase, which looks like the "breathing of the cell." Fu et al. demonstrated that the pressure evolution is caused by the inhomogeneous distribution of ions concentration in the electrodes. Cycling a Li-ion cell at a high current means intercalation/de-intercalation of lithium ions in a short time, which leads to a large concentration gradient of ions inside the electrodes structure.[31]

### 1.2.3 Research question

The main goal of this thesis work is to understand how the breathing and swelling mechanisms are connected to the thermal parameters of a Li-ion battery cell. In particular, it first deals with a thermal characterization, through a software simulation (COMSOL Multiphysics), of the lithium-ion cells with an existing device and compares the values obtained from the simulation with those of the experiments. In this way, it is possible to understand the sources of error in the laboratory but also in the simulation. However, the drawback of the existing device is that the study of the thermal behavior of the Li-ion battery cells does not consider how the volume change can affect the thermal parameters. So, the general idea is to measure the temperature distribution and the heat flux of the cell under testing, varying boundary conditions (pretension force, SoC, contact pair). Applying an external mechanical load and temperature gradient on a test bench, the questions behind the modeling of the device are:

- How does the heat flux sensor react?
- Which is the maximum pretension value that the heat-flux sensor can stand?
- Changing pretension force and temperature values, is the sensor's output always the same?

That is why this work will show a suitable method and a new structure to answer to these questions.

### 1.2.4 Thesis outline

The contents of this Thesis are organized as presented in the following.

The present chapter (the first) explains the mechanisms of breathing and swelling and their causes and consequences. In addition, it gives a brief description of the composition and working principle of a lithium-ion battery.

The second chapter illustrates the state of the art of lithium-ion batteries, which are the thermal parameters to consider, how they change during the charge and discharge cycles. Finally, five experiments present in the literature for the thermal characterization of a cell are illustrated.

The third chapter illustrates the working principle of the heat flux sensor, which is one of the protagonists of the present work.

The fourth chapter compares the thermal values of different lithium-ion cells from an experimental and a simulation point of view. Subsequently, to recreate the different scenarios of geometric changes of the cell due to breathing and swelling and to understand how the thermal parameters are connected with them, it is possible to apply an external force on it. However, in the current device previously considered among the various sensors involved, there is the heat flux sensor. Furthermore, it is in this regard that the present work considers this sensor and analyzes its behavior. Expressly, modeling and simulation of a new device can guarantee stability and robustness, avoiding the heat flux sensor break when different values of pretension force at different values of temperature are applied.

Finally, the fifth chapter represents the concluding chapter, which shows some considerations on expanding the modeled device in this thesis for future experiments in the laboratory.



# Chapter 2

## State of the art

This chapter briefly explains the heat flux and its related parameters such as thermal conductivity, capacity, and thermal diffusivity. The work carried out in the literature on different methods measuring the main thermal parameters of Li-ion cells is summarized. Different methods are described and compared to each other considering application purpose, setup effort, accuracy, battery type, and results.

Heat flux measurement is used in heat transfer to quantify the transfer of heat within systems. Several techniques are in common use, including calorimetric methods involving a heat balance analysis; differential temperature sensor such as a thermopile, the most common type of heat flux sensor, which is precisely the device examined in this thesis and on which the chapter 3 is focused. The method is performed by measuring a temperature difference without knowing thermal conductivity or thermal resistance. These parameters do not have to be known since the heat flux sensor enables an in-situ measurement of the existing heat flux by using the **Seebeck effect**. However, heat flux sensors have to be calibrated to relate their output signals to heat flux values. Once the heat flux sensor is calibrated, it can directly measure heat flux without the rarely known value of thermal resistance or thermal conductivity.

### 2.1 Theory

During the charging and discharging processes inside the battery, heat is generated. Therefore, it is essential to measure the heat transfer and/or heat flux with their related thermal parameters. In general, to analyze a lithium-ion battery in working condition in its entirety, it is necessary to consider

mechanical behavior and its thermal behavior.

To study the thermal behavior of a lithium-ion battery cell, it is worth defining all the different thermal parameters and the operating conditions of a lithium-ion battery.

Lithium-ion performs well at elevated temperatures, but prolonged exposure to heat reduces longevity. Therefore, manufacturers of Li-ion battery usually gives the operating temperature of lithium-ion battery to range from 0°C to 45°C for charging operations and -20°C to 60°C for discharging operations (as shown in the following table).

Battery type	Charge temperature	Discharge temperature	Charge Advisory
Lead acid	-20°C to 50°C	-20°C to 50°C	Charge at 0.3C or less below freezing. Lower V-threshold by 3mV/°C when hot.
NiCd, NiMH	0°C to 45°C	-20°C to 65°C	Charge at 0.1C between -18°C and 0°C. Charge at 0.3C between 0°C and 5°C. Charge acceptance at 45°C is 70%. Charge acceptance at 60°C is 45%.
Li-ion	0°C to 45°C	-20°C to 60°C	No charge permitted below freezing. Good charge/discharge performance at higher temperature but shorter life.

Table 2.1: Temperature range for different battery types [20]

However, Figure 2.1 highlights that the optimal temperature range for lithium-ion battery operation is between 15°C to 35°C. Once the temperature is out of these comfortable regions, LIBs will degrade fast with an increased risk of facing safety problems that include fire and explosion. In general, impacts from temperature can be divided into two categories: low-temperature effects and high-temperature effects. Such low temperatures will affect the performance and life of LIBs. At these low operating temperatures, LIBs will show slow chemical-reaction activity and charge-transfer velocity, which leads to the decrease of ionic conductivity in the electrolytes and lithium-ion diffusivity within the electrodes. Such a decrease will result in the reduction of energy and power capability and sometimes even performance failure. At the same time, the high internal temperature is caused by heat generation inside the LIBs, which happens at high current state, including operations with a fast-charging rate and fast discharging rate. The high-temperature effects will also lead to the performance degradation of the batteries, including the loss of capacity and power. Generally, the loss of lithium and the reduction of active materials under high temperatures will result in the loss

of capacity, while the increase of internal resistance is responsible for the loss of power. Hence, batteries operate over a wide temperature range, but this does not give permission to also charge them under these conditions. The charging process is more delicate than discharging, and special care must be taken. Extreme cold and high heat reduce charge acceptance; thus, the battery must be brought to a moderate temperature before charging. [32][33]

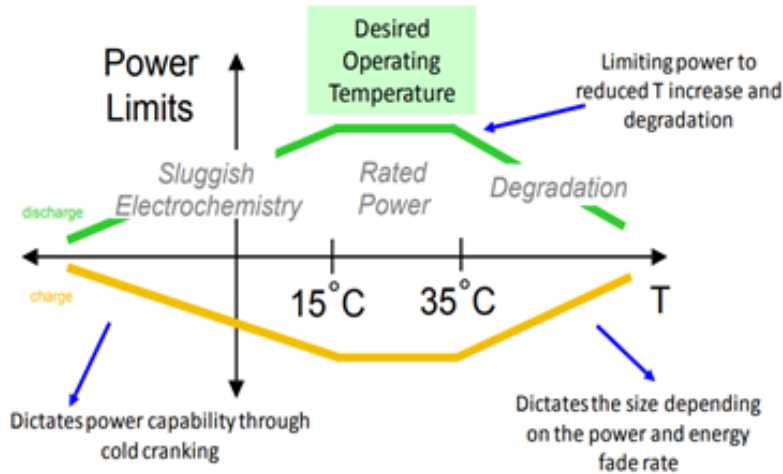


Figure 2.1: Graph Temperature-Power Limits of LIB[9]

Another aspect to consider is the electrolyte inside the lithium-ion battery and see how it is related to the temperature. Liquid electrolytes in lithium-ion batteries consist of lithium salts in an organic solvent. A liquid electrolyte acts as a conductive pathway for the movement of cations passing from the negative to the positive electrodes during discharge. Typical conductivities of liquid electrolyte at room temperature (20°C) are in the range of 10 mS/cm, increasing by approximately 30–40% at 40°C and decreasing slightly at 0°C. So, with high temperature for the ions is easier to move from one side to the other, and this means that when the temperature increases, the ionic conductivity of the electrolytes also increases. [34]

The main thermal parameters to be considered for the lithium-ion battery are heat flux density, and thermal conductivity.

### 2.1.1 Definition of thermal parameters

**Heat flux:** Temperature differences in a given system induce a heat flux. The induced heat flux always flows from the hot to the cold side. So, the

heat flux, sometimes also referred to as heat flux density, is a flow of energy per unit of area per unit of time. Usually is indicated as  $\dot{q}$  and in SI, its units are  $\text{W}/\text{m}^2$ . For most solids in usual conditions, heat is transported by conduction, and the heat flux is adequately described by Fourier's law.

$$\dot{q} = -k \frac{dT(x)}{dx} \quad (2.1)$$

Where:

- $\dot{q}$ : heat flux [ $\text{W}/\text{m}^2$ ]
- $k$ : thermal conductivity [ $\text{W}/(\text{mK})$ ]
- $\frac{dT(x)}{dx}$ : temperature gradient in the direction of the flow [ $\text{K}/\text{m}$ ]

Fourier's law in one dimension differential form: [2.1](#)

**Thermal conductivity:** often denoted by  $k$  or  $\lambda$ , it refers to the intrinsic ability of a material to transfer or conduct heat. It is one of the three methods of heat transfer. Heat transfer processes can be quantified in terms of appropriate rate equations. The rate equation in this heat transfer mode is based on Fourier's law of heat conduction:

$$\dot{Q} = kA \frac{\Delta T}{t} \quad (2.2)$$

Where:

- $\dot{Q}$ : flow rate heat transfer [ $\text{W}$ ]
- $k$ : thermal conductivity [ $\text{W}/(\text{mK})$ ]
- $A$ : cross-sectional area [ $\text{m}^2$ ]
- $\Delta T$ : temperature difference [ $\text{K}$ ]
- $t$ : thickness [ $\text{m}$ ]

The thermal conductivity equation can be calculated using the following:

$$k = \frac{\dot{Q}t}{A\Delta T} \quad (2.3)$$

Hence, thermal conductivity is the property of a material to transfer heat by conduction from an area of high temperature ( $T_1$ ) to an area with a lower

temperature ( $T_2$ ). It is defined as the amount of thermal energy that flows per unit of time through a unit area of a material when a temperature gradient exists perpendicular to this area. The thermal conductivity of a Li-ion cell is highly orthotropic because of its layered construction, as shown in the figure. The thermal conductivity can be classified in:

- in plane-thermal conductivity
- through-plane thermal conductivity

They depend on the direction of heat transfer. Through-plane means in the direction perpendicular to the plane, while in-plane means in the direction along the plane.

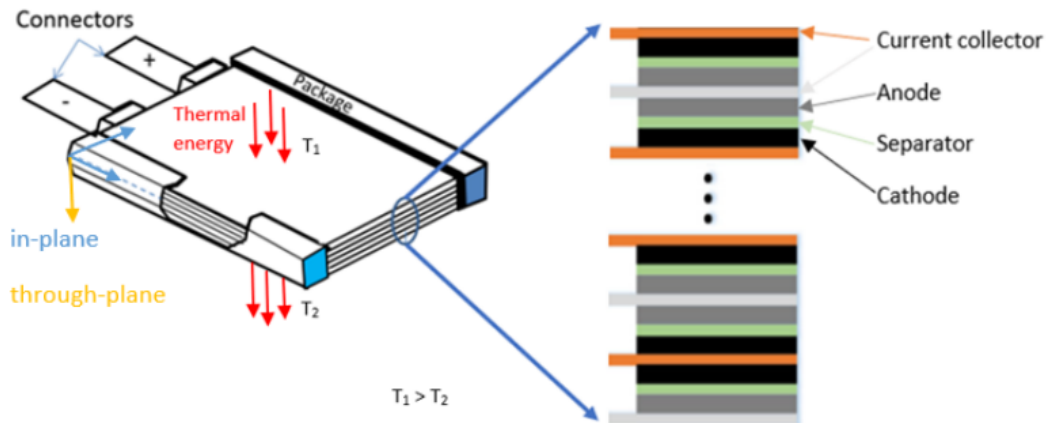


Figure 2.2: Structure of Li-ion pouch cell[10][11]

## 2.2 Thermal characterization of the cell: review of literature

### 2.2.1 I experiment [2]

The Institute for Development of Mechatronic Systems, NTB Interstate University of Applied Sciences of Technology, developed an experiment to have an estimation of the thermal properties of a battery cell. To do this, they used an active measuring unit consisting of a temperature and heat flux density sensor and a Peltier element. These temperature/heat flux sensing (THFS) units are uniformly arranged around a battery cell. In this study, the term

thermal behavior includes system parameters such as thermal conductivity ( $\lambda$ ) or heat capacity ( $c_p$ ) of the cell itself, but also the amount of heat that is generated inside the cell during a given load profile. Therefore, the test rig described in this paper can acquire and control heat flux and temperature distribution on the surface of prismatic and pouch cells. In order to do the set of experiments, the cell under test is surrounded by 87 uniformly distributed temperature/ heat flux sensor (THFS) units, which are in contact with the battery cell on one side while connected to a heat sink on the other side. The heat sink consists of an aluminum block with integrated cooling channels through which a coolant with the fixed temperature  $T_{sink}$  is circulated. So, the principal job of the THFS units is to measure the surface temperature of the device under test, as well as the heat flux density flowing from the sample towards the heat sink or vice versa.

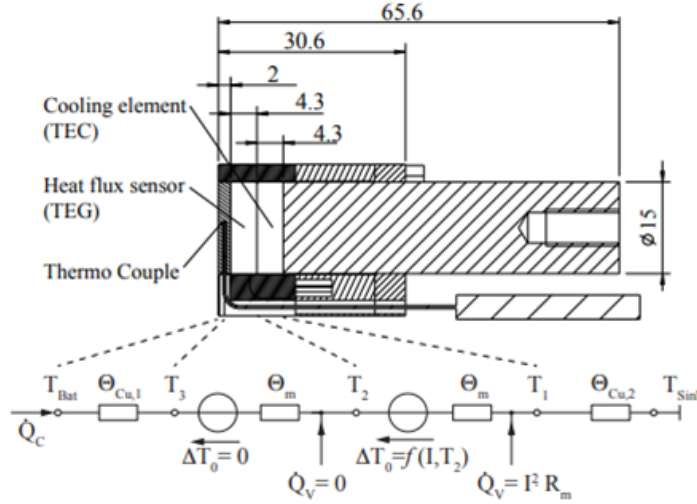


Figure 2.3: Cross-sectional view of the developed THFS unit with its corresponding equivalent circuit model (ECM) as used for the one-dimensional thermal analysis[2]

This temperature/heat flux sensor unit, as shown in the figure, is composed of two copper parts, one thermo-couple and two thermo-electric cooler/generator (TEC/TEG).

The cell under test is a prismatic cell with physical dimensions of 175 mm x 125 mm x 45 mm.

In this experiment, a lithium manganese oxide (LMO) cell is tested. For

the characterization measurement, all THFS units are operated with a constant temperature, which means that the whole surface of the cell is held constant at 25°C. The cell is cycled at a rate of 2C, from 10% to 80% SoC (State of Charge). The post-processing and visualization of the measurement data conducted in MATLAB are shown in Figure 2.4.

It is possible to see the measured heat flux distribution after 60 min at a steady state with all 87 THFS units operated in temperature-controlled mode. Based on these results, they arrived at these conclusions:

- the heat fluxes on the side faces as well as on the bottom side are close to zero;
- the main part of the heat flux is almost uniformly released through the large front and rear side;
- the largest heat flux is measured near the positive terminal of the battery cell.

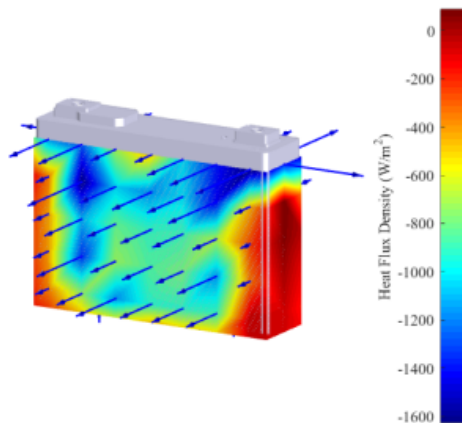


Figure 2.4: Measured heat flux density for a cell after 60 min cycling loading with 2C-rate and actively controlled surface temperature of 25°C[2]

Therefore, a fairly good heat dissipation within the yz-plane (Figure 2.5) as well as towards the electrical terminals can be expected. Another interesting result is the observed asymmetry between the two electrical terminals.

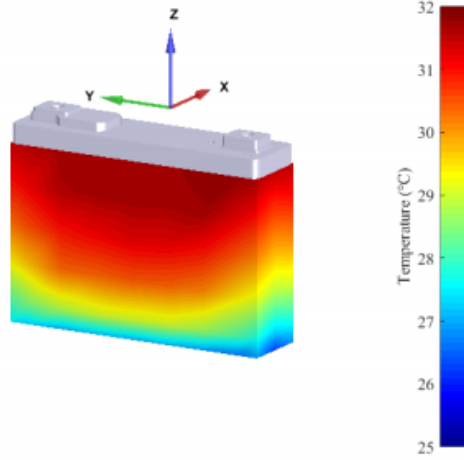


Figure 2.5: Measured temperature distribution of the prismatic battery cell with a constant temperature of 25°C on the bottom side and continuous 2C loading[2]

All the values are illustrated in the following table:

Position	Heat Flux Density	Surface Area
Side face (negative)	219 $W/m^2$	5625 $mm^2$
Side face (positive)	295 $W/m^2$	5625 $mm^2$
Bottom side	119 $W/m^2$	7875 $mm^2$
Front side	964 $W/m^2$	21.875 $mm^2$
Rear side	952 $W/m^2$	21.875 $mm^2$

Table 2.2: Average heat flux density on the different sides of the battery cell at  $t = 60$  min [2]

### 2.2.2 II experiment [3]

In this study, a new method is used to measure simultaneously both the thermal conductivity and the capacity of a battery that employs commonly available electrochemical equipment without using a calorimeter. This new method is called thermal impedance spectroscopy (TIS). It examines the transfer behavior between internal heat generation and resulting battery surface temperature in the frequency domain.

The new method adopts the concept of thermal impedance as a complete characterization of a system's thermal properties. The thermal impedance function is analogous to the electrical impedance. It can be evaluated for a set of given frequencies as complex numbers, representing a thermal impedance spectrum. The thermal impedance spectrum gives indications about the contributions of different parts of the system to heat transfer and allows detection of the relative changes of thermal properties. Due to the mathematical similarity to the electrical model, the thermal impedance function can be derived similarly to the electric impedance function, essentially using the Ohm and Kirchhoff laws. In this approach, heat flow is treated as a current equivalent and temperature gradient as a voltage equivalent.

To demonstrate the applicability of the proposed method in a real experiment environment and to obtain thermal impedance spectra for Li-ion batteries, they used a potentiostat/galvanostat with a digital signal processor (DSP) for signal generation and data acquisition. The system is known as the BPS 1000FL Powergraphy Battery Parameterization System. The batteries under test are cylindrical Li-ion batteries of the 18650 type with a specified capacity of 1500 mAh. In order to apply a constant heat flow to the surface of the batteries, a heating band made of Ni-Fe alloy with a total resistance of around  $5\Omega$  and a negligible change in this value over the experimental temperature range are tightly wound around the battery, as shown in the figure:

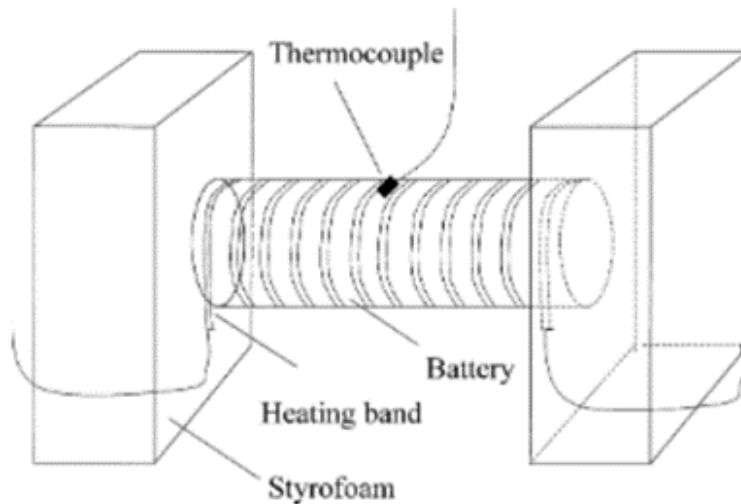


Figure 2.6: Experimental set-up for thermal impedance measurement on cylindrical battery using external heating coil for generating heat pulse[3]

A thermocouple is fixed at the mid-point of the battery so that it touched the surface of the battery but not the heating band. The battery is compressed between two plates of thermal insulator (porous polystyrene) to minimize heat conduction along the battery axis and through its sides.

To increase the transfer of heat from the battery surface and, thereby, decrease the largest thermal time constant of the system, a CPU-cooler fan is placed 1 cm from the battery to provide convection cooling. Specific values of the thermal parameters have been calculated using information about battery dimensions and weight, and all the values are obtained by the fit of their thermal impedance spectra to thermal impedance function:

Manufacturer	$h_{rc}$ (W/(Km <sup>2</sup> ))	$C_c$ (J/(K g))	$h_c$ (W/(Km <sup>2</sup> ))	$C_T$ (J/K g)	$k_T$ (W/(K m))
Moly Energy	109.3	1.1	-	1.8	0.9
Panasonic	137.1	1.1	302.1	1.9	1.4
Hitachi	84.5	1.1	269.3	1.2	2.8
Samsung	140.2	1.1	-	2.4	1.2

Table 2.3: Heat transfer coefficients, specific heat and thermal conductivity of cylindrical Li-ion batteries [3]

It is interesting to notice that the Xenon-Flash method by Maleki et al. and other reported methods of thermal characterization are generally extensive, cost-intensive, and cell destructive. TIS is a new non-destructive method of thermal characterization of battery cells. The analysis is executed in the frequency domain. Impedance spectroscopy is a standard tool to examine the transfer behavior of systems in a widely spread field of science. Especially in the sector of battery technology, impedance spectroscopy reached high importance for the analysis of the electrochemical impedance of battery cells at different ambient and load conditions. A primary advantage of analyzing the frequency domain spectrum of system response is the possibility to clearly separate the influences of physical effects with differing time constants that occur simultaneously in the time domain. The technical procedure of TIS exhibits several analogies to electrochemical impedance spectroscopy (EIS). It examines the thermal transfer behavior of a battery cell in the frequency domain. The thermal impedance function can be obtained directly from time-domain response to heat excitation without any presumption about the internal structure of the circuit as given in the equation:

$$Z_t(s) = \frac{L\{T(t)\}}{L\{i(t)\}} \quad (2.4)$$

Where  $L\{\}$  is a Laplace transform,  $T(t)$  is a temperature response function, and  $i(t)$  is an excitation function in the time domain, like a heat pulse.[35]

### 2.2.3 III experiment[4]

In this experiment are reported experimental thermal property data of the Sony US-18650 cylindrical lithium-ion cell. The properties in question are specific heat capacity ( $c_p$ ), thermal diffusivity ( $\alpha$ ), and thermal conductivity ( $k$ ) in the presence and absence of electrolyte. It is noticed that the in-plane  $k$  value (measured along with layers) is nearly one order of magnitude higher than the cross-plane  $k$  at an open-circuit voltage (OCV) of 2.75 V and 3.75 V. Two different methods of measuring  $c_p$  are used: transient temperature measurement and adiabatic calorimetry. Similarly, two methods are used to obtain the thermal conductivity values. In the first method, the cross-plane  $k$  is determined by applying a known heat flux across the surface of the cell and sampling the temperature difference at known locations. In the second method, both cross-sectional and in-plane thermal conductivity values are calculated from cross-plane and in-plane thermal diffusivity:

$$\alpha = \frac{k}{\rho c_p} \quad (2.5)$$

Direct steady-state measurement: Figure 2.7 shows the experimental setup used to measure the thermal conductivity directly using a heat flux perpendicular to the plane of the layers. The heating assembly is a form of a terminal resistor. Current is supplied by a DC power supply and voltage measured by a microvoltmeter. Sample layers, each having an area comparable to that of the heater surface, are placed in contact with both sides of the heater assembly, with a thin flathead type E thermocouple inserted between them. High-thermal conductivity paste is applied between sample layers, and layers are sandwiched between rectangular blocks of Styrofoam. This assembly is placed in a two-part press with internal rims at the top and bottom to apply pressure to the sample layers. To ensure good thermal contact, the upper and lower halves of the Plexiglas press are compressed firmly at their four corners by means of through bolts. The heat flow generated by the heater (supplied with a constant current) is directly perpendicular to the plane of the layers.

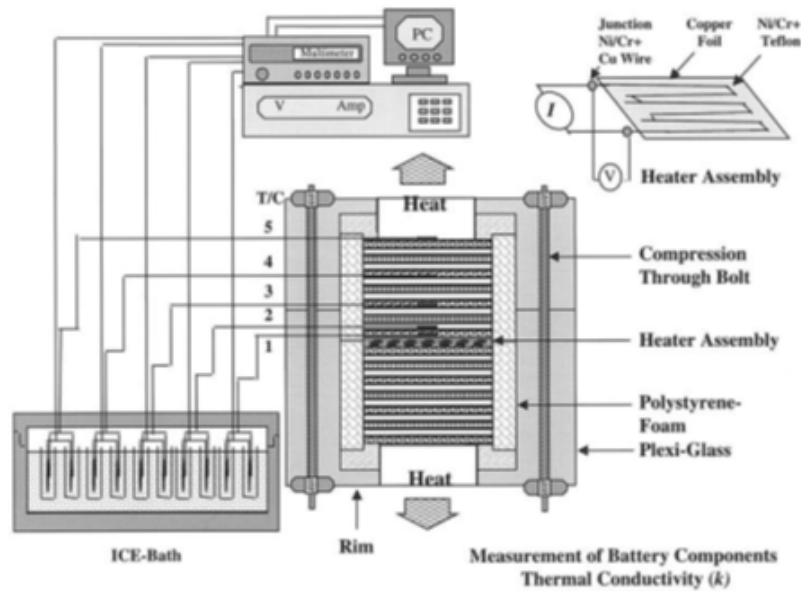


Figure 2.7: Setup[4]

### Xenon Flash Technique (XFT)

The Xenon Flash Method is usually used for measuring thermal diffusivity. If the thermal diffusivity is known, the thermal conductivity can be calculated by multiplying this parameter, the specific density, and the specific heat capacity.

The principle of the flash method is to heat the front surface of the sample with a short pulse of a xenon flash and to record the temperature rise at the rear face by a thermal imaging camera. The cell and heating sources are in a temperature chamber. The thermal diffusivity can be calculated from the sample thickness and the time of temperature rise, according to the one-dimensional unsteady heat conduction.

Maleki used the XFT as a second method to measure through-plane and in-plane thermal conductivities of a cylindrical  $LiCoO_2$  cell with and without electrolyte. For these measurements, the samples are cut to disk and rectangular shapes, and for the measurements, with electrolyte, they are transferred back into a glove bag for adding electrolyte. For the through-plane thermal conductivity, the heat pulse is directed perpendicularly to the planar surface of disk-shaped sample layers, and for the in-plane thermal conductivity, the heat pulse is directed parallel to the planar surface of the rectangular sample

layers. The specific density and specific heat capacity are calculated from mass-fraction-weighted values for each component taken from datasheets. Two sets of measurements are conducted:

1. the heat pulse is directed perpendicularly to the planar surface of disk-shaped samples of the layered components or assemblies. In this set, it is possible to measure the through-plane thermal conductivity;
2. the heat pulse is directed parallel to the planar surface of the rectangular sample layers, stacked to form a parallelepiped. In this set, it is possible to measure the in-plane thermal conductivity.

The final data of the experiments are:

Materials	In-plane $C_p$ (J/g K)	Cross-plane $C_p$ (J/g K)	In-plane $\alpha$ $cm^2/s$ OCV: 2.45/3.75 (V)	Cross-plane $\alpha$ $cm^2/s$ OCV: 2.45/3.75 (V)	In-plane k (W/mK) OCV: 2.45/3.75 (v)	Cross-plane k (W/mK) OCV: 2.45/3.75 (V)
PE	0.602	0.601	0.115/0.116	0.0124/0.0133	21.57/21.75	2.33/2.49
NE	0.598	0.623	0.090/0.156	0.0088/0.0119	8.72/15.11	0.89/1.20
PE/Sp/NE	1.088	11.089	0.0071/0.099	0.0076/0.0095	17.69/24.66	1.90/2.36
PE/Sp/NE + electrolyte	1.278	1.280	0.058/0.079	0.0099/0.0100	20.06/28.05	3.39/3.40

Table 2.4: In-plane and cross-plane thermal properties of Sony US-18650 lithium-ion battery components with and without electrolyte [4]

### 2.2.4 IV experiment[5]

Bazinski modified an isothermal calorimeter and used it as a heat flow meter to measure the through-plane thermal conductivity of a lithium-iron-phosphate (LFP) pouch cell as a function of its temperature and state of charge (SoC). The calorimeter is composed of two aluminum plates, each connected in parallel to a water bath, acting as heat exchangers. The pouch cell is placed between these two heat exchangers. Each heat exchanger, whose base surfaces are surrounded by aerogel insulation to minimize heat loss with the surrounding air, keeps the cells' face at a controlled temperature. These temperatures are different from each other. Therefore a temperature gradient between the cell faces is established, and heat flows across its thickness. The heat flux is detected by heat flux sensors (thermopiles) which are placed between the pouch cell and heat exchangers on both sides. An electric motor connected to the upper heat exchanger also allows controlling the pressure on

the pouch cell. Measurements are taken at three different cell surface temperature levels ( $-5^{\circ}\text{C}$ ,  $25^{\circ}\text{C}$ , and  $55^{\circ}\text{C}$ ) as well as three different SoC levels (0%, 50% and 100%) to determine if these parameters had any effect on the through-plane thermal conductivity.

An assumption used in the calculation of thermal conductivity with re-configured calorimeter is that the convective heat flux is uniform across the exposed surface of the platens.

This study does not investigate in-plane thermal conductivity because the design of the reconfigured calorimeter does not lend itself to this type of measurement. The two heat exchanger platens cannot be spaced apart enough to accommodate the height or width of the pouch cell.

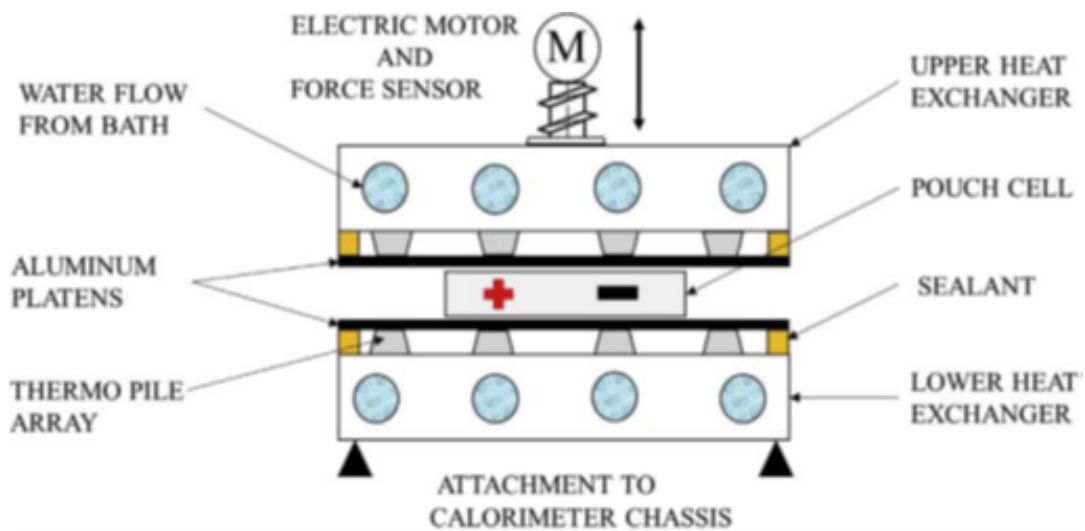


Figure 2.8: Schematic of the isothermal calorimeter[5]

Isothermal calorimeters are designed to maintain the battery at a constant preset temperature (Figure 2.8). The heat transfer is detected by highly sensitive thermopiles, which are placed between the cell and heat exchangers.

The figure below shows the through-plane thermal conductivity of the cell as a function of cell surface temperature for three values of SoC (0%, 50%, 100%). The through-plane thermal conductivity is independent of the cell temperature ( $-5$ - $55^{\circ}\text{C}$ ) across its full SoC range.

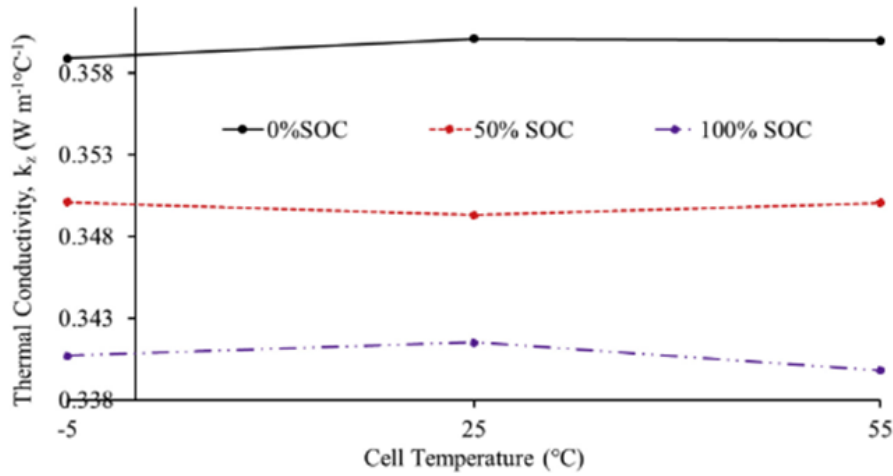


Figure 2.9: Through-plane thermal conductivity of the cell as a function of temperature for different SoC levels[5]

### 2.2.5 V experiment [6]

The aim of this experiment is to define thermal parameters, such as heat capacity and through-plane thermal conductivity of pouch-type cells. Application of local heat flux measurement with a gradient heat flux sensor (GHFS) is adopted to determine the cell thermal parameters in different surface points of the cell. This method is not destructive, and it is also less expensive than the other methods mentioned above.

So, this method provides an opportunity to determine the thermal conductivity of pouch cells in the thickness direction, which is perpendicular to the current collector, and the specific heat capacity by a single experiment. The experiment does not require a steady-state mode at a certain temperature. Moreover, the cell thermal parameters can be determined in a short period of time. In the method, a simple external heat source is used. The incoming and out-coming heat fluxes are measured by two GHFSs. The temperature is measured by temperature sensors placed in the proximity of the GHFSs. The cell under test is a high-power Li-ion pouch cell with dimensions 256 mm x 259 mm x 12.7 mm; lithium titanate (LTO) cell is considered as the test cell. Since the thickness of the pouch cell is usually much smaller than the dimensions of the flat surface, it is possible to consider a pouch LTO cell

as an infinite plate with anisotropic thermal parameters. Hence, the determination of the thermal parameters in an infinite plate can be considered a one-dimensional task if a uniform heat flux through the plate is generated.

The performed experiment is shown in the following figure:

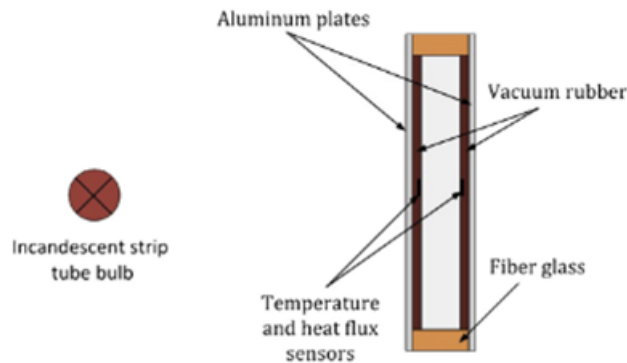


Figure 2.10: Test setup[6]

Temperature and heat flux sensors are installed on both sides of the cell. The cell with sensors is squeezed by two aluminum plates, which increase the uniformity of the heat flux. Vacuum rubber is placed between the cell and the aluminum plates in order to compensate surface imperfections and remove air between the aluminum plates and the pouch cell. The other surfaces of the cell, which are not in contact with the vacuum rubber (has a low thermal conductivity), are thermally insulated by fiberglass. This is necessary for the generation of the heat flux only in one direction through the aluminum plates, vacuum rubber, and pouch cell. A 500 W electric incandescent strip tube bulb is used to produce the heat flux through the system, and it can be used as a constant heat flux source. The aluminum plate closest to the lamp is painted black to increase its emissivity. The minimum time of the experiment is equal to 290 s. The thermal parameters are measured for different SoC and in different points of the cell surface, which is perpendicular to the current collectors. The SoC is varied from 10% to 90% with 20% steps. The thermal parameters are measured in three points on the cell surface with the following coordinates given in meters: (0.116, 0.216), (0.116, 0.129), and (0.116, 0.04). The results of the experiments are given in the table below.

Points	Parameters	SoC=10%	SoC=30%	SoC=50%	SoC=70%	SoC=90%
First point	k, W/mK	0.614	0.671	0.735	0.704	0.652
	$C_p$ , K/kgK	1043.6	1066.7	1067.7	1058	1052.5
Second point	k, W/mK	0.633	0.631	0.687	0.635	0.594
	$C_p$ , J/kgK	1020	1030.1	1053.7	1062	1052.5
Third point	k, W/mK	0.653	0.647	0.651	0.657	0.649
	$C_p$ , J/kgK	1033.1	1035.6	1039.2	1035.7	1032.0

Table 2.5: Thermal parameters of the Li-ion pouch cell[6]

### 2.2.6 Comparison between the methods

Method	Battery type	Advantages	Disadvantages
1st[2]	LMO pouch/prismatic cells	Ability to acquire and control heat flux and temperature distribution on the surface of the cell.	Large number of sensors exposed to a possible external force applied.
2nd[3]	18650 type cylindrical cell	Separate the influences of physical effects with differing time constants that occur simultaneously in the time domain. Non-destructive. Computation of thermal conductivity and capacity.	Not suitable for other types of lithium-ion cell.
3rd[4]	18650 type cylindrical cell	High accuracy.	Destructive.
4th[5]	LFP/NMC pouch cell	Ability to measure the specific heat capacity and the through-plane thermal conductivity as functions of temperature and SoC.	The design is not able to measure the in-plane thermal conductivity.
5th[6]	LTO pouch cell	Non-destructive. Does not require deep discharge of the cell.	The design is not able to measure the in-plane thermal conductivity.

Table 2.6: Comparison between thermal characterization methods

In all the methods found in the literature cited above, there is the characterization from the thermal point of view of different lithium-ion cells, both with different chemical compositions and with different geometries. Therefore, it is possible to notice how the values of heat flux and thermal conductivities in the three directions can be calculated and vary with different SoC, C-rate, temperature, and open-circuit voltage. However, these methods do not deal

with how the thermal behavior and, therefore, the various values that have been calculated (such as heat flux, thermal conductivity) can change as a function of a volumetric change of the cell. As previously written, during its life cycle made up of continuous charges and discharges, the cell undergoes breathing and swelling processes. Therefore, it is essential to introduce the mechanical study and its influence on the thermal study within these methods. In none of these methods, except with some structural changes, is it possible to apply a load in such a way as to exert an external force and simulate breathing and swelling mechanisms. To make up for this gap, this thesis has tried to remodel an already existing device, which will be explained later in the 4 chapter, to consider the breathing and swelling phenomena, which are not yet covered by the literature.

# Chapter 3

## Heat flux sensor

### 3.1 Working principle of the heat flux sensor

Among the different devices that have been classified in the methods listed in the chapter 2, there is one which is the subject of this work: heat flux sensor, specifically the FHF02. A heat flux sensor is a transducer that generates an electrical signal proportional to the total heat rate applied to the surface of the sensor. The measured heat rate is divided by the surface area of the sensor to determine the heat flux.

The sensor FHF02 is a thermopile. This thermopile measures the temperature difference across the polyamide body of FHF02. Working completely passive, the thermopile generates a small voltage that is a linear function of this temperature difference. The heat flux is proportional to the same temperature difference divided by the effective thermal conductivity of the heat flux sensor body. To know the output of the sensor, the user needs an accurate voltmeter that works in the millivolt range. To convert the measured voltage,  $U$ , to a heat flux  $\Phi$ , the voltage must be divided by the sensitivity  $S$ , a constant that is supplied with each individual sensor.

$$\Phi = \frac{U}{S} \tag{3.1}$$

Considering the Figure 3.1 to explain the working principle of a heat flux sensor.

Heat flux sensors generally have the shape of a flat plate and a sensitivity in the direction perpendicular to the sensor surface. Usually, several thermocouples connected in series, called thermopiles, are used.

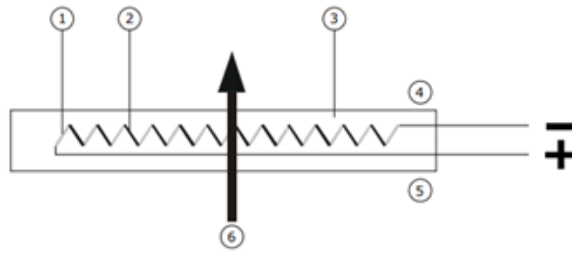


Figure 3.1: General working principle of heat flux sensor[12]

Each thermocouple consists of two metal alloys marked 1 and 2. The general advantages of thermopiles are their stability, low ohmic value (which implies little pickup of electromagnetic disturbances), good signal-noise ratio, and the fact that zero input gives zero output. Disadvantageous is the low sensitivity. A single thermocouple generates an output voltage that is proportional to the temperature difference between its hot-and cold joints. Putting thermocouples in series amplifies the signal. In a heat flux sensor, the hot-and cold joints are located at the opposite surfaces 4 and 5. In steady-state, the heat flux 6 is a linear function of the temperature difference across the sensor and the average thermal conductivity of the sensor body, 3. The thermopile generates a voltage output proportional to the heat flux through the sensor. The exact sensitivity of the sensor is determined at the manufacture by calibration and can be found in the datasheet.[12]

The sensitivity of the sensor is defined as the slope of the output characteristic curve ( $\Delta Y/\Delta X$ ) or, more generally, the minimum input of physical parameter that will create a detectable output change.

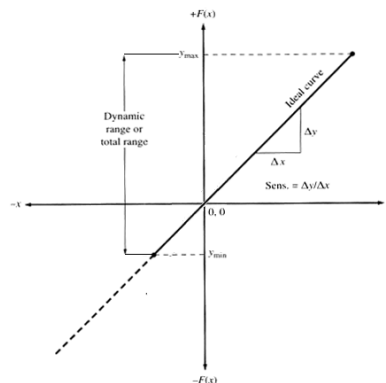


Figure 3.2: Ideal curve of a sensor[13]

### 3.1.1 Calibration

In order to do in-situ measurements, the user must be provided with the correct calibration constant  $S$ . This constant is also called sensitivity. The sensitivity is primarily determined by the sensor construction and operation temperatures but also by the geometry and material properties of the object that is measured. Therefore, the sensor should be calibrated under the condition that is close to the conditions of the intended applications. While heat flux sensors are typically supplied with sensitivity by the manufacturer, there are times and situations that call for a re-calibration of the sensor. Especially when the heat flux sensors cannot be removed after the initial installation. To perform the re-calibration of the sensor, some come with an integrated heater with specified characteristics. By applying a known voltage on and current through the heater, controlled heat flux is provided, which can be used to calculate the new sensitivity.[12]

$$S = \frac{U}{\Phi} \quad (3.2)$$

The thermocouple integrated into the sensor FHF02 is of type T. Type T (copper-constantan) thermocouples are suited for measurements in the  $[-200,350]^{\circ}\text{C}$  range. They are very stable thermocouples and are often used in extremely low-temperature applications such as cryogenics or ultra-low freezers.

A thermocouple is an electrical device consisting of two dissimilar electrical conductors forming an electrical junction. A thermocouple produces a temperature-dependent voltage because of the Seebeck effect, and this voltage can be interpreted to measure temperature.

Seebeck effect is a thermoelectric effect, and it is the direct conversion of temperature to electric voltage and vice versa via a thermocouple. A thermoelectric device creates a voltage when there is a different temperature on each side. Conversely, when a voltage is applied to it, heat is transferred from one side to the other, creating a temperature difference. This effect can be used to generate electricity, measure temperature, or change the temperature of objects. The Seebeck effect refers to the development of an electromotive force across two points of an electrically conducting material when there is a temperature difference between those two points. Under open-circuit conditions where there is no internal current flow, the gradient of voltage ( $\nabla V$ )

is directly proportional to the gradient in temperature ( $\nabla T$ ):

$$\nabla V = -S(T)\nabla T \quad (3.3)$$

Where  $S(T)$  is a temperature-dependent material property known as the Seebeck coefficient.

In contrast to most other methods of temperature measurement, thermocouples are self-powered and require no external form of excitation. The main limitation with thermocouples is accuracy; system errors of less than one degree Celsius ( $^{\circ}\text{C}$ ) can be difficult to achieve.

The standard configuration for thermocouple usage is shown in the following figure. The desired temperature  $T_{sense}$  is obtained using three inputs—the characteristic function  $E(T)$  of the thermocouple, the measured voltage  $V$ , and the reference junctions' temperature  $T_{ref}$ . The solution to the equation  $E(T_{sense}) = V + E(T_{ref})$  yields  $T_{sense}$ . [14]

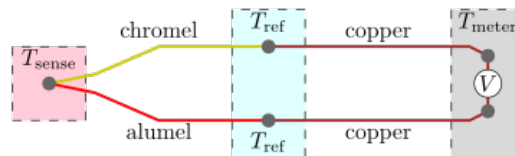


Figure 3.3: K-type thermocouple (chromel–alumel) in the standard thermocouple measurement configuration. [14]

# Chapter 4

## Modeling & Simulation

This chapter shows the realization of an *NMC* (Nickel, Manganese, and Cobalt) battery using the COMSOL Multiphysics software, the replication of the experiment described in “*In Situ Measurement of Orthotropic Thermal Conductivity on Commercial Pouch Lithium-Ion Batteries with Thermoelectric Device*” of Luigi Aiello et al.[15] and the comparison of the results to see the difference between experimental values and ideal values. Secondly, the modeling and the simulation of the device designed to analyze the heat flux sensor’s behavior under different pretension forces and different temperatures values are shown.

The following simulations have been carried out through simulation software with the FEA (*Finite Element Analysis*) technique.

### 4.1 Validation of the model with data from the thermal characterization of Li-ions cells with existing device

In this paragraph, the experiment from the paper “*In Situ Measurement of Orthotropic Thermal Conductivity on Commercial Pouch Lithium-Ion Batteries with Thermoelectric Device*” of Luigi Aiello et al.[15] is described. This experiment aims to measure the thermal conductivity in the three directions, the in-plane and through-plane thermal conductivities of batteries obtained from a fully electric vehicle commercialized in 2016. The idea consists of forcing a thermal gradient on the battery along the desired direction and measuring the heat flux and temperature after the steady-state condition

has been reached.

The batteries under test are laminate pouch-type cells, obtained from a disassembled pack contained 24 identical battery modules, each of which consisted of eight 41 Ah Li-ion pouch cells with cut-off voltage limits of 2.5 V and 4.2 V and a nominal voltage of 3.7 V. The manufacturer defines the energy density for one cell to be 174 Wh/kg. The nominal dimensions of one battery are 290 mm x 216 mm x 8 mm with a total weight of about 800 g. As far as the chemistry is concerned, graphite is used as anode material, and the cathode material is a spinel of NMC (Nickel-Manganese-Cobalt) and LMO (Lithium-Manganese Oxide). The current collector to the side of the anode is made of copper, while the current collector to the cathode side is made of aluminum. Finally, the chemical composition of the electrolyte is identified as  $LiPF_6$  dissolved in a carbonate-mixture solvent.



Figure 4.1: Reference system used for the orientation of the orthotropic thermal conductivity measurements. The “w” vector is on the battery thickness direction, “v” vector is parallel to the tabs direction, and “u” vector is perpendicular to them [15]

The battery contained 22 anode layers, 21 cathode layers, and 44 separator foils. The following table contains values for the measured thicknesses of all battery components:

Component	Thickness ( $\mu\text{m}$ )	Component	Thickness ( $\mu\text{m}$ )	Component	Thickness ( $\mu\text{m}$ )
Anode	140	Cathode	170	Separator	20
Anode CC	10	Cathode CC	20	Pouch	190
Anode AM	65	Cathode AM	75		

Table 4.1: Thicknesses of Single Layer Component Samples, Prepared by the BIB-Cutting Method [21]

The determination of the orthotropic thermal conductivity required three measurements for its determination along with the three spatial directions. In general, a temperature gradient is forced along the direction of the thermal conductivity measurement, and the thermal insulation is designed to avoid temperature gradients in the other directions. To create the temperature gradient on the top of the battery cell, two mat heaters are placed. In contrast, on the bottom, a cooling device is placed, it is made of a milled 15 mm thick aluminum plate and 12 Peltier cells homogeneously distributed under it to obtain a stable temperature lower than the ambient one even after hours of testing. The heat subtracted from the aluminum plate during operation is exhausted through a group of extruded aluminum heatsinks.

The measurement of the heat flux was performed with foil heat flux sensors (model FHF02) produced by the company “*Hukseflux Thermal Sensors.*”

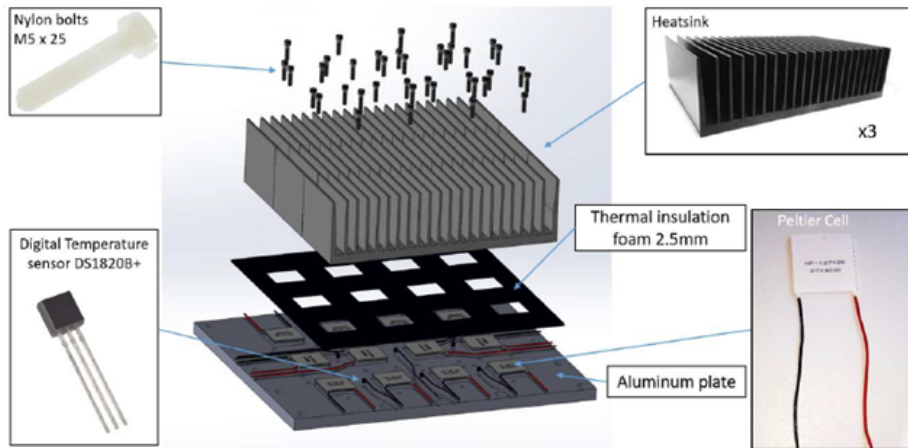


Figure 4.2: General assembly of temperature-guarded plate (Peltier plate). The heatsinks were fixed to the aluminum plate with nylon bolts in order to increase the efficiency of the system. Digital temperature sensors DS1820B+ with 0.5 C uncertainty were placed inside the aluminum plate volume. [15]

For the measurements, three battery samples are used. The samples are all fresh and all set with an SoC of 30%.

For the measurement along the “w” direction, the temperature gradient is forced along the thickness direction; the cooling device provided a constant temperature of about 10°C, and the mat heaters placed on top of the object provided a constant heat generation until the steady-state condition is reached without exceeding the maximum temperature limit of 50°C. The scheme of the test bench is reported in Figure 4.3. The pertinax foil provided a homogeneous thermal resistance between the aluminum plate on the bottom and the cell, avoiding the generation of temperature gradient along with the longitudinal directions. With this condition, it is possible to consider the battery as an infinite plane and apply the following equation:

$$\sigma = \frac{\text{SurfaceHeatFlux}(W/m^2) \cdot \text{Thickness}(m)}{\Delta\text{Temperature}(K)} \quad (4.1)$$

The heat flux used in the Equation 4.1 is the average between the top and the bottom sensor measurements. The temperature difference is the temperatures on top and bottom of the cell measured by the thermocouples integrated into the heat flux sensors.

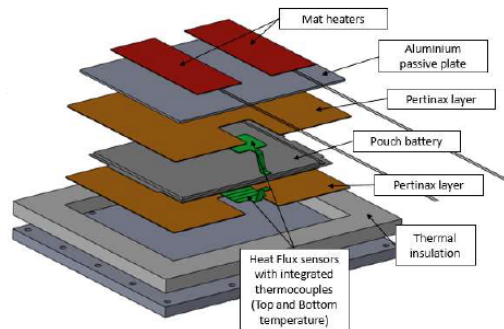


Figure 4.3: Test bench [15]

The measurements in the plane are based on the same principle. In this case, the test bench is modified. Two additional L-shaped aluminum blocks are mounted on the aluminum plate to allow the vertical mounting of the battery.

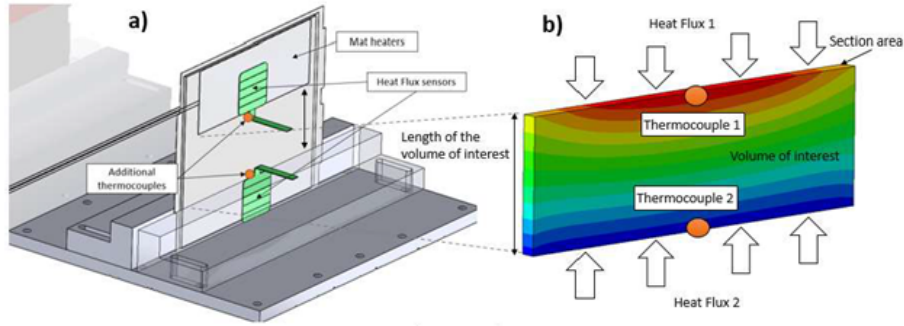


Figure 4.4: Schematic diagram showing the expected heat flux for the measurement of the thermal conductivity along the longitudinal directions. [15]

The structure is modified in order to apply a temperature gradient across the longitudinal directions. Also, the system is symmetric with respect to the third direction, which is why a temperature gradient along the thickness direction is not expected.

For the thermal conductivity calculation, the volume of interest is the one between the lower edge of the mat heaters and the upper edge of the L-shaped connectors (Figure 4.4). The equation is:

$$\sigma(W/mK) = \frac{\text{AveragedHeatFlux}(W) \cdot \text{LenVol.Int}(m)}{\Delta\text{Temperature}(K) \cdot \text{SampleSection}(m^2)} \quad (4.2)$$

This experiment was taken as a reference to be able to analyze the thermal behavior (heat flux and thermal conductivity in the three directions) also from a simulative point of view and, subsequently, to be able to modify the current device used in such a way as to make it suitable for the application of an external force and simulate the effects of breathing and swelling phenomena.

#### 4.1.1 Simulation of the experiment

The experiment explained above was replicated on COMSOL Multiphysics in order to do the simulation and compare the experimental results with the simulated ones.

To model the thermal behavior of the Li-ion battery cell, a 3D single-layer approach is adopted, and two out of three batteries of the experiment were considered.

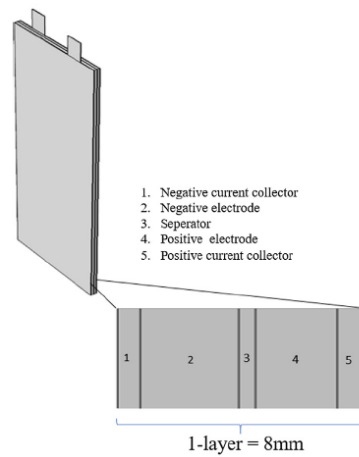


Figure 4.5: Schematic of a 3D single-layer cell [16]

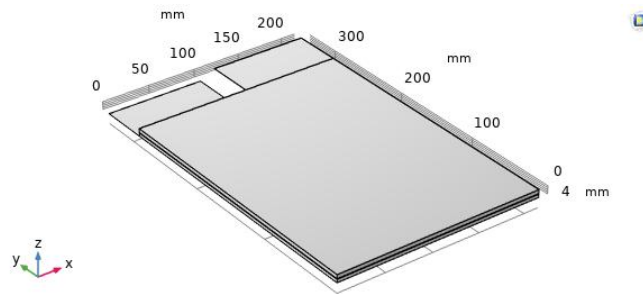


Figure 4.6: Simulated 3D single-layer pouch cell

In this approach, using the finite element simulation software, a 3D model of a single-layer cell is developed. All the electrochemical and thermal equations are solved using the software, and a two-way approach is used for coupling the electrochemical and thermal modules. In this approach, the heat generation rates due to electrochemical reactions, entropy change, and joule heating are calculated locally with the multiphase electrochemical model. Then, the 3D thermal solver used heat generation to find the temperature field in the battery cell. The models for the “through-plane” and for the “in-plane” measurements are shown in the following figure:

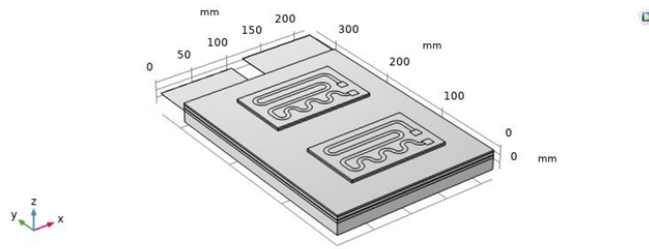


Figure 4.7: Simulated test bench in "w" direction (top view)

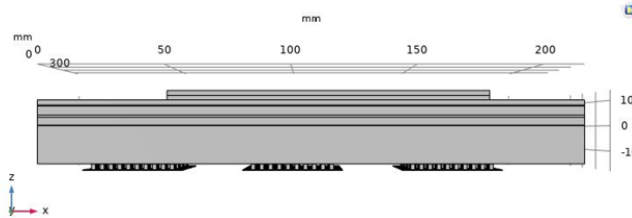


Figure 4.8: Simulated test bench (side view)

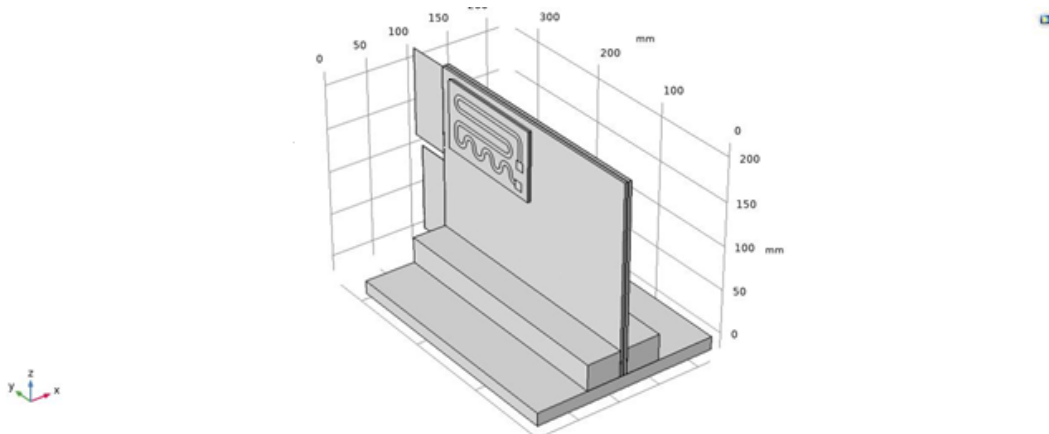


Figure 4.9: Simulated test bench in longitudinal directions

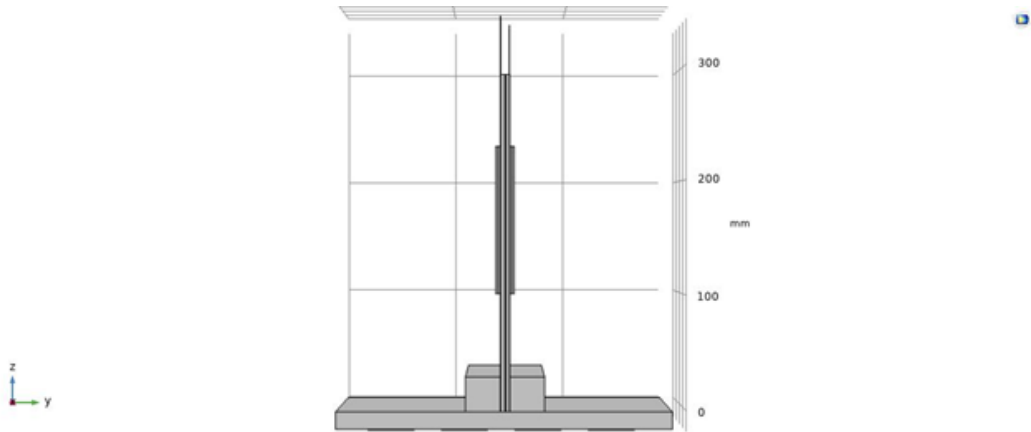


Figure 4.10: Simulated test bench in longitudinal directions (side view)

Regarding the Peltier cell, it consists of several thermoelectric legs sandwiched between two thermally conductive plates, one cold and one hot. The device that needs to be cooled down must be attached to the cold face.[17]

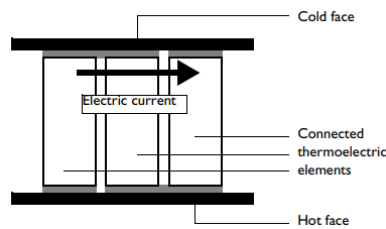


Figure 4.11: Schematic of a Peltier cell [17]

Exploiting the Peltier effect, an electrical current from one extremity of the thermoelectric elements networks to the opposite extremity generates an orthogonal heat flux, causing a temperature difference between the plates. The embedded model used the equations for the thermoelectric effect and the heat conduction for the electrical conductor and ceramics.

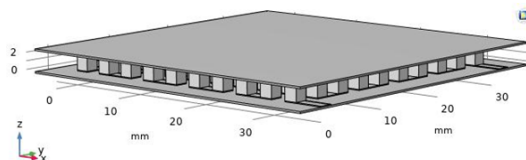


Figure 4.12: Peltier cell (external view)

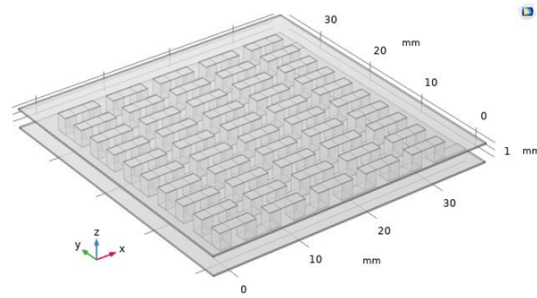


Figure 4.13: Peltier cell (internal view)

The figure below shows an example of the measured temperature on the two plates of the Peltier cell:

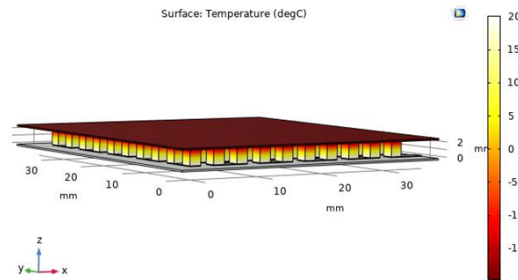


Figure 4.14: Surface temperature Peltier

The dimension of the Peltier cell is 40 mm x 40 mm, and it was made by referring to the various Peltier cells on the website of "*RS Components*".[36]

Regarding the mat heater, "*Heating Circuit: Layered Shell Version*" [18] on the COMSOL website was taken as a reference to realize the model.

Mat heater is a small heating circuit, and it consists of an electrically resistive layer deposited on a glass plate and covered with a silicon layer. The layer causes Joule heating when a voltage is applied to the circuit. The layer's properties determine the amount of heat produced. The realized model simulated the electrical heat generation and the heat transfer. Hence, the model used the Heat Transfer in Shells interface of the Heat Transfer Module in combination with the Electric Currents. A drawing of the modeled heating circuit is shown in the following figure:

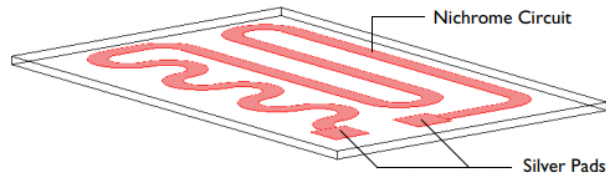


Figure 4.15: Drawing of the heating circuit deposited on a glass plate [18]

The device consists of a serpentine-shaped Nichrome resistive layer,  $10\ \mu\text{m}$  thick and  $5\ \text{mm}$  wide deposited on a glass plate ( $130\ \text{mm} \times 80\ \text{mm} \times 2\ \text{mm}$ ) and successively covered with a silicon layer ( $130\ \text{mm} \times 80 \times 2\ \text{mm}$ ). At each end, it has a silver contact pad measuring  $10\ \text{mm} \times 10\ \text{mm} \times 10\ \mu\text{m}$ .

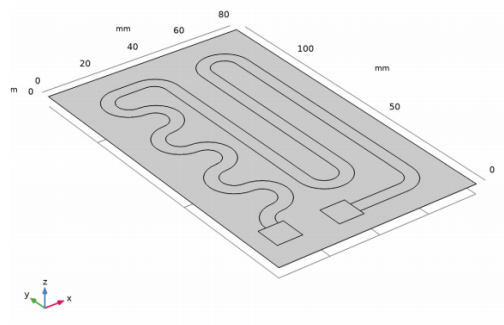


Figure 4.16: Mat heater [18]

## 4.1.2 Results

In this section, the results of the experiment and the simulation are shown and compared.

It is possible to see how the steady-state condition is almost equal for both cases, and it is around 30 minutes of testing.

The following graphs and tables show the measurements along with the three directions ( $w$ ,  $u$ ,  $v$ ) of the sample batteries 2 and 3. Sample 1 was not simulated because it has the same geometry as sample 2.

4.1 – Experiment with existing device

	Sample	Thermal conductivity (W/mK)	Top Heat Flux ( $W/m^2$ )	Bottom Heat Flux ( $W/m^2$ )	$\Delta T$ ( $^{\circ}C$ )	Thickness (m)
Experiment [15]	2	0.76	876.49	1093.86	10.37	0.008
Experiment [15]	3	0.84	1041.26	1084.30	9.52	0.0077
Simulation	2	0.75	1050.2	873.848	10.49	0.00817
Simulation	3	0.94	1035.75	1071.93	8.6	0.0077

Table 4.2: Experimental and simulated measurements in "w" direction - Sample 2 and 3

	Sample	Thermal conductivity (W/mK)	Abs. Top HF (W)	Abs. Bottom HF (W)	$\Delta T$ ( $^{\circ}C$ )	LenVol.Int (m)	Sample Section ( $m^2$ )
Experiment [15]	2	25.77	15.85	10.77	22.87	0.085	0.00192
Experiment [15]	3	25.69	15.38	11.20	23.80	0.085	0.001848
Simulation	2	24.53	16.53	8.85	22.9	0.085	0.00192
Simulation	3	33.00	15.78	10.04	18	0.085	0.001848

Table 4.3: Experimental and simulated measurements in "v" direction - Sample 2 and 3

	Sample	Thermal conductivity (W/mK)	Abs. Top HF (W)	Abs. Bottom HF (W)	$\Delta T$ ( $^{\circ}C$ )	LenVol.Int (m)	Sample Section ( $m^2$ )
Experiment [15]	2	24.80	15.27	8.03	33.75	0.115	0.0016
Experiment [15]	3	26.58	6.61	4.83	16.06	0.115	0.00154
Simulation	2	28.98	17.42	8.84	32.58	0.115	0.0016
Simulation	3	26.08	6.62	4.85	16.43	0.115	0.00154

Table 4.4: Experimental and simulated measurements in "u" direction - Sample 2 and 3

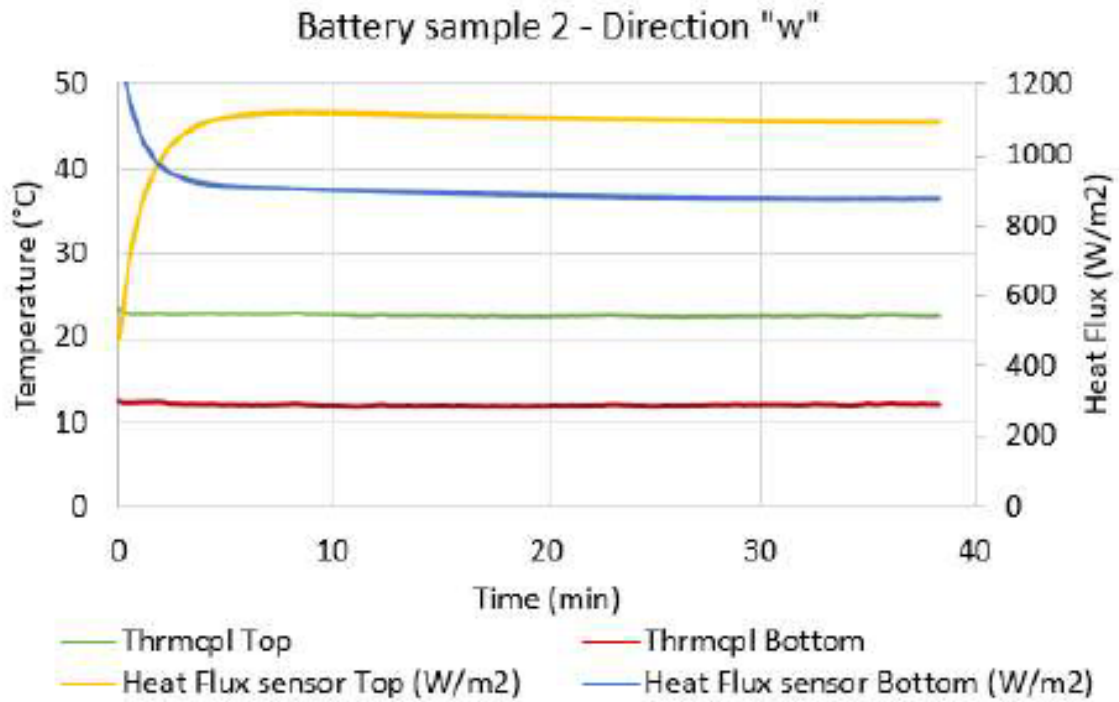


Figure 4.17: Experimental plots relative to sample 2 in "w" direction [15]

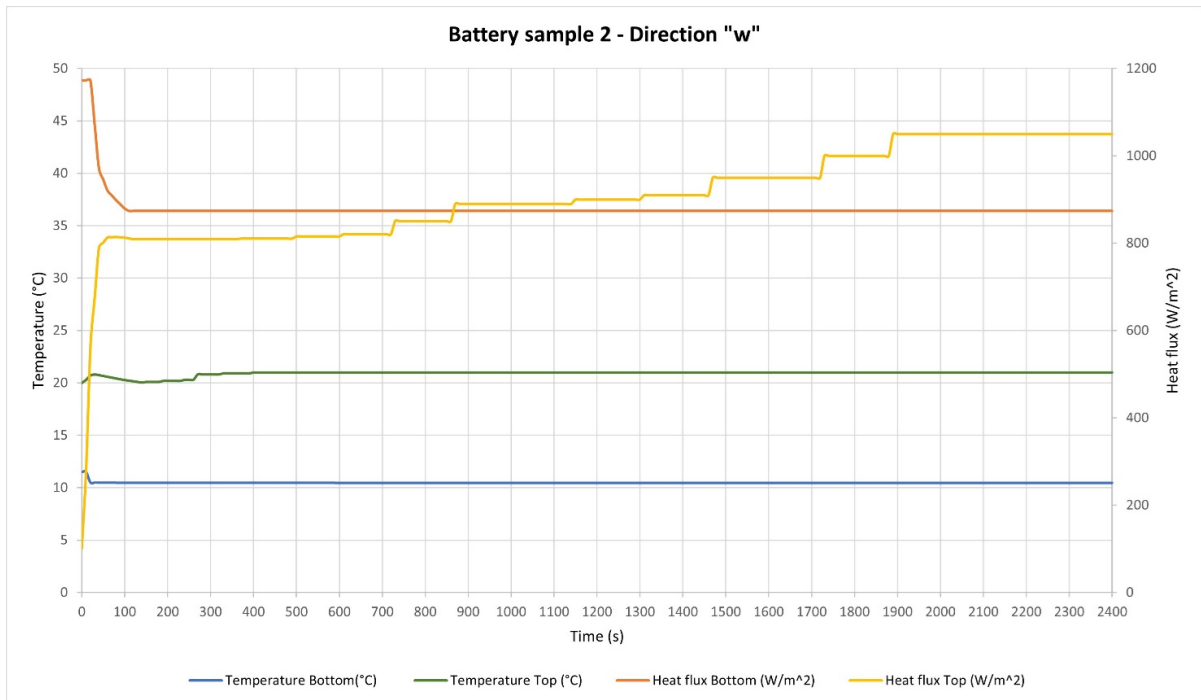


Figure 4.18: Simulated plots relative to sample 2 in "w" direction

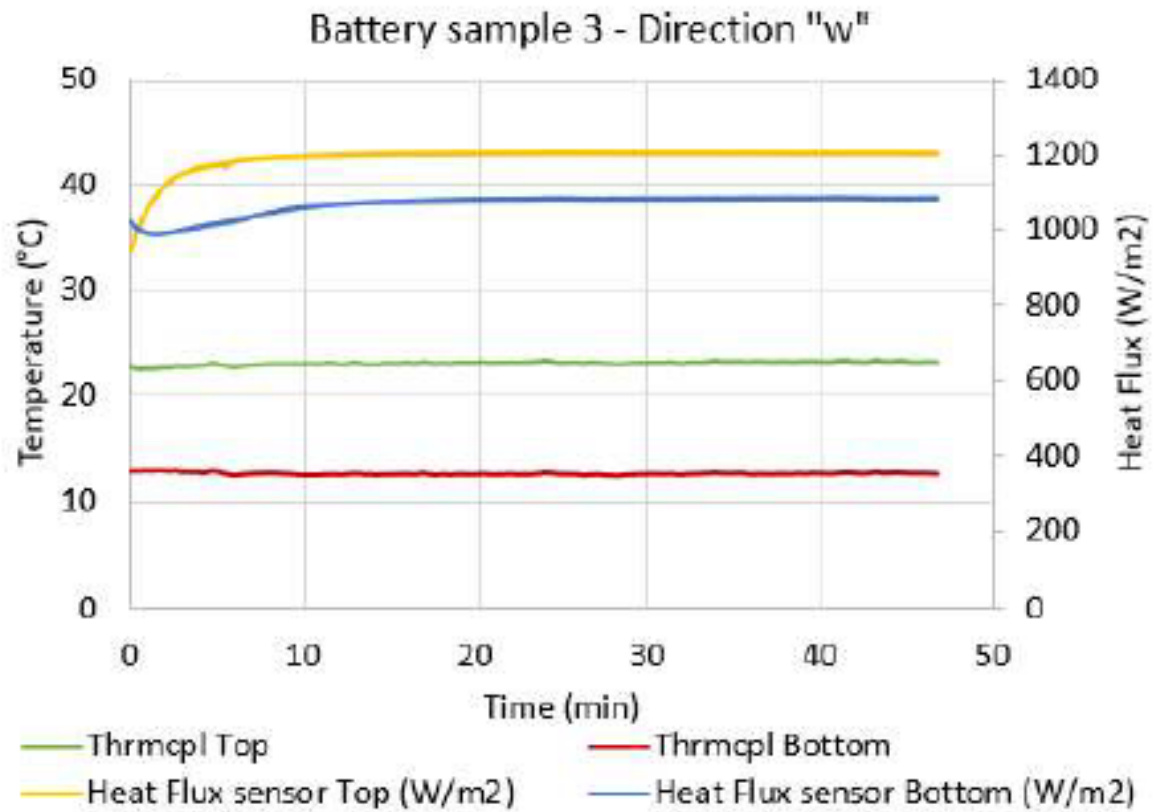


Figure 4.19: Experimental plots relative to sample 3 in "w" direction [15]

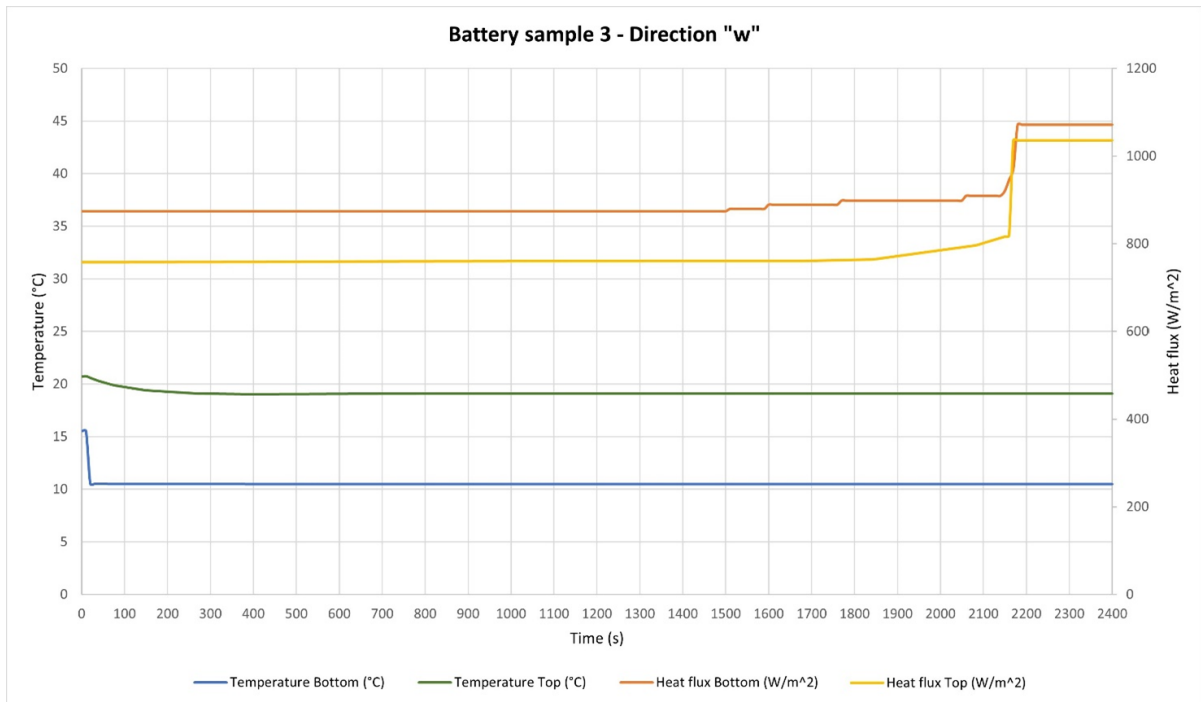


Figure 4.20: Simulated plots relative to sample 3 in "w" direction

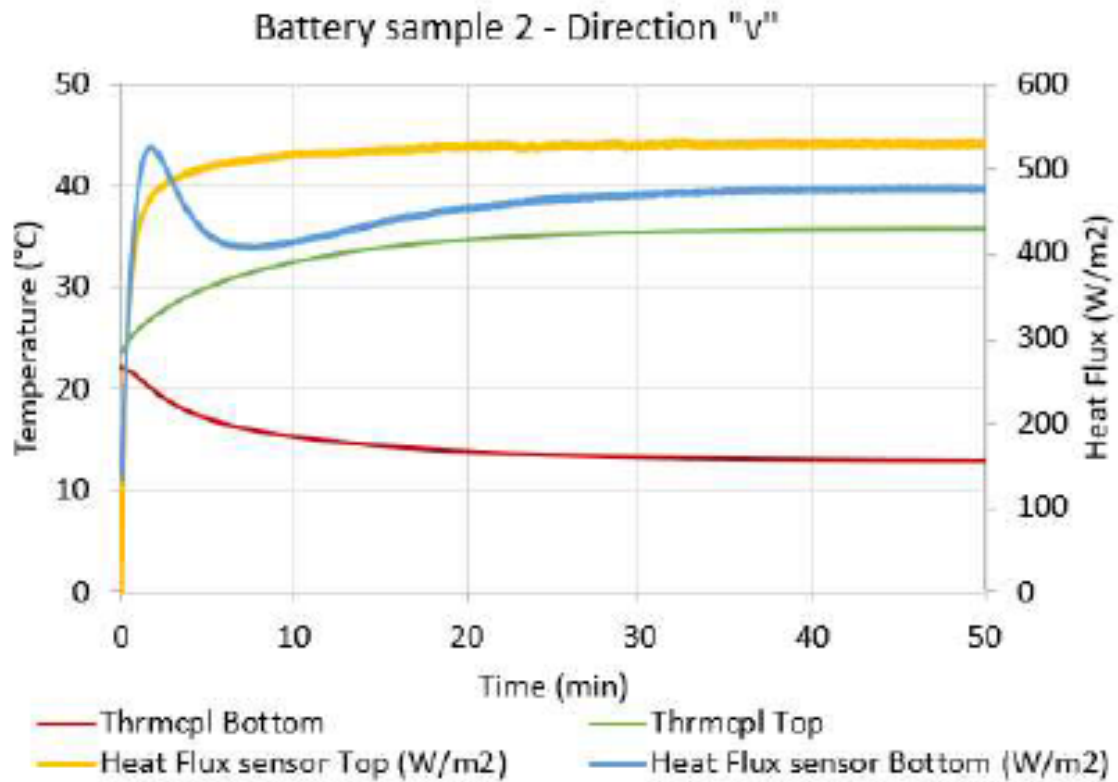


Figure 4.21: Experimental plots relative to sample 2 in "v" direction [15]

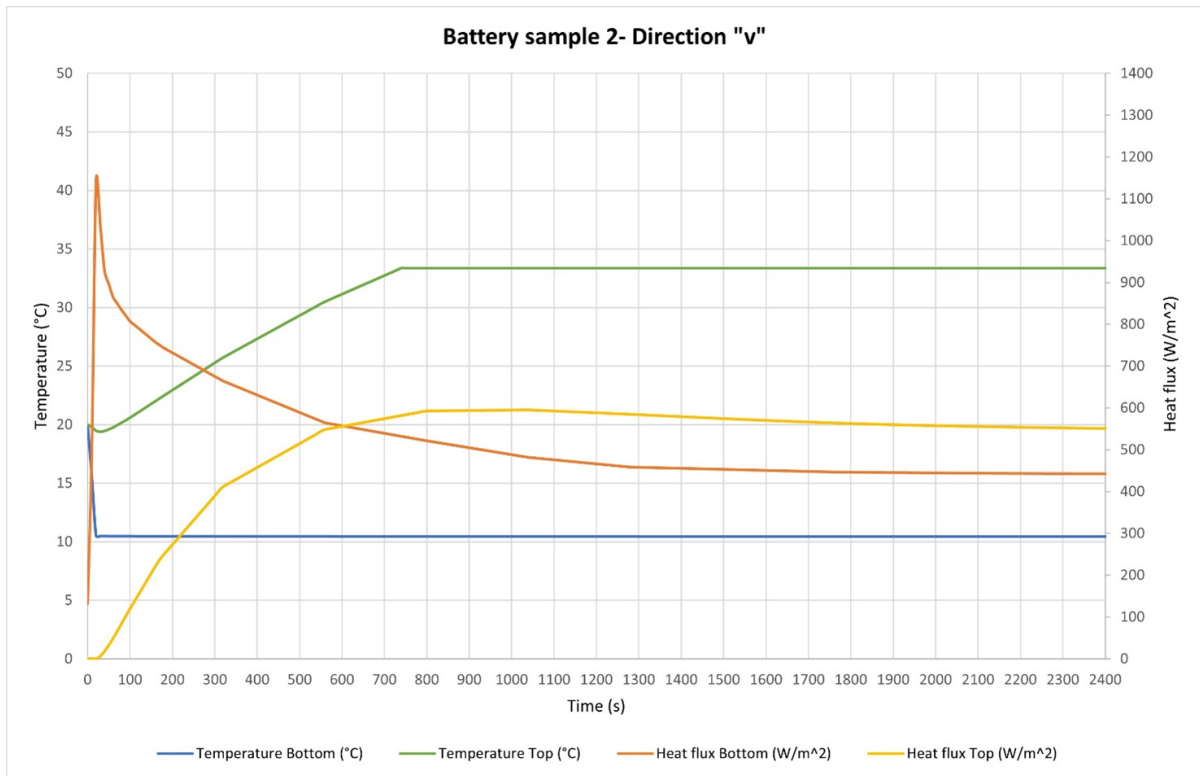


Figure 4.22: Simulated plots relative to sample 2 in "v" direction

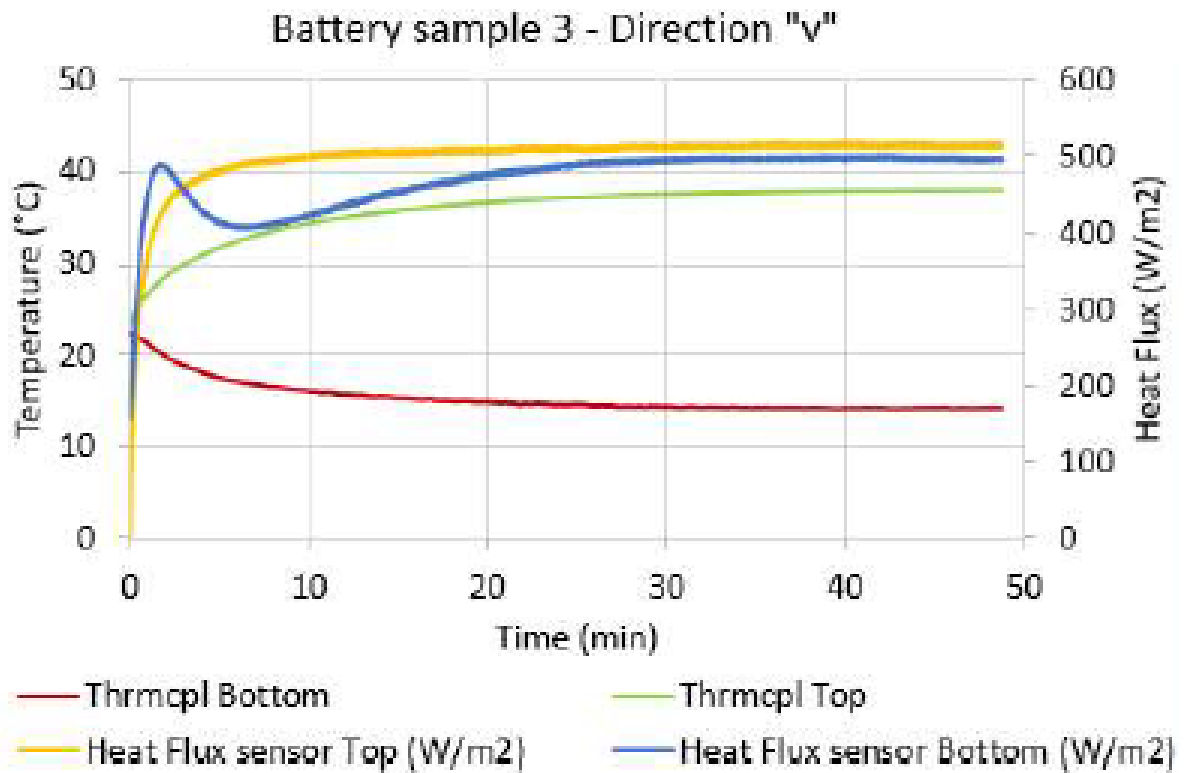


Figure 4.23: Experimental plots relative to sample 3 in "v" direction [15]

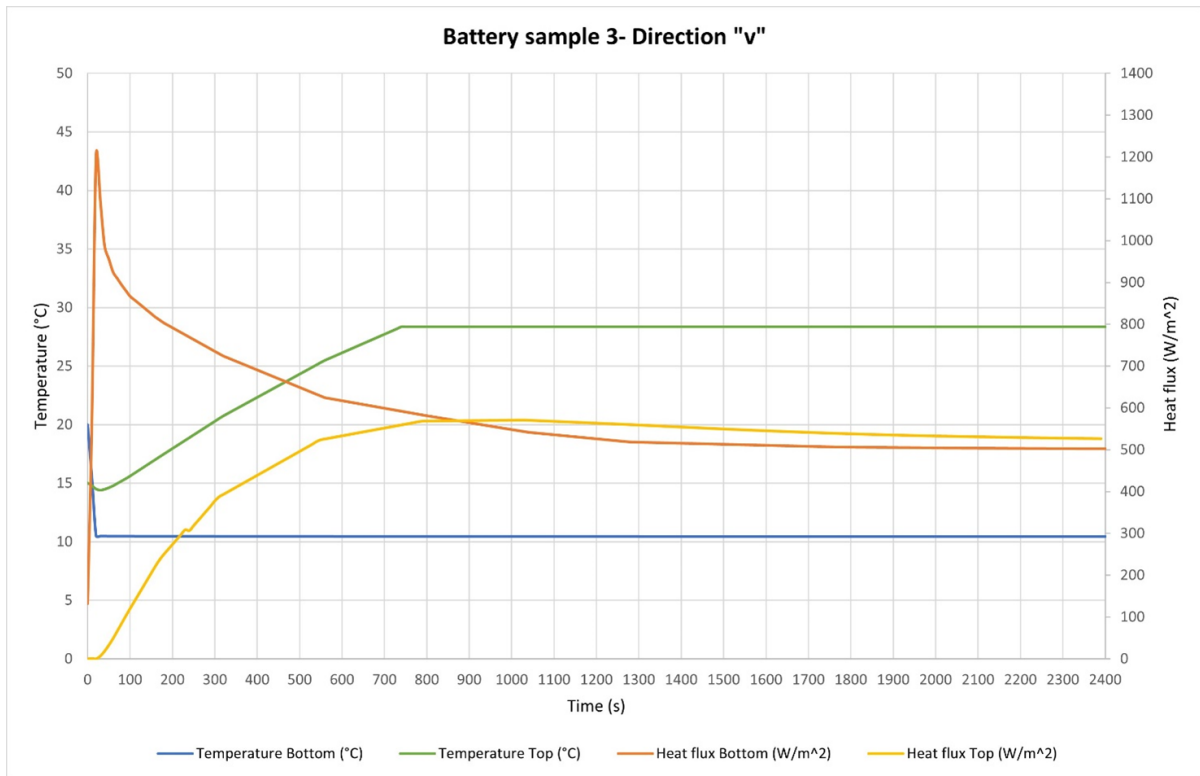


Figure 4.24: Simulated plots relative to sample 3 in "v" direction

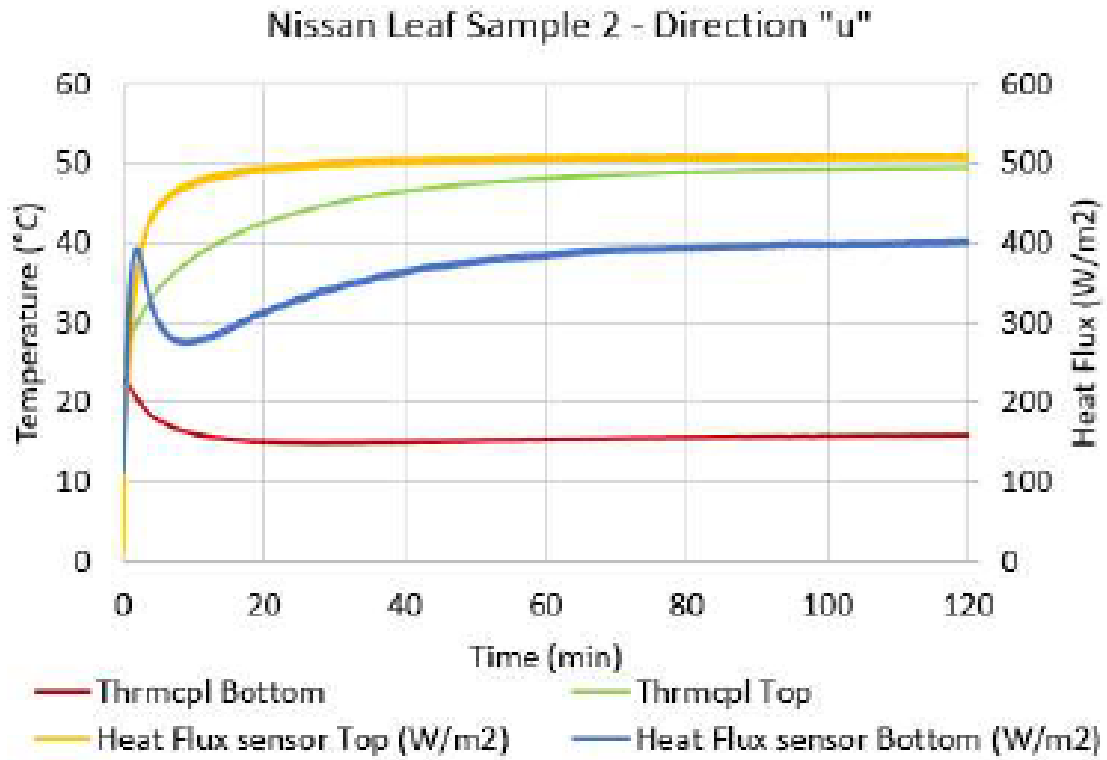


Figure 4.25: Experimental plots relative to sample 2 in "u" direction [15]

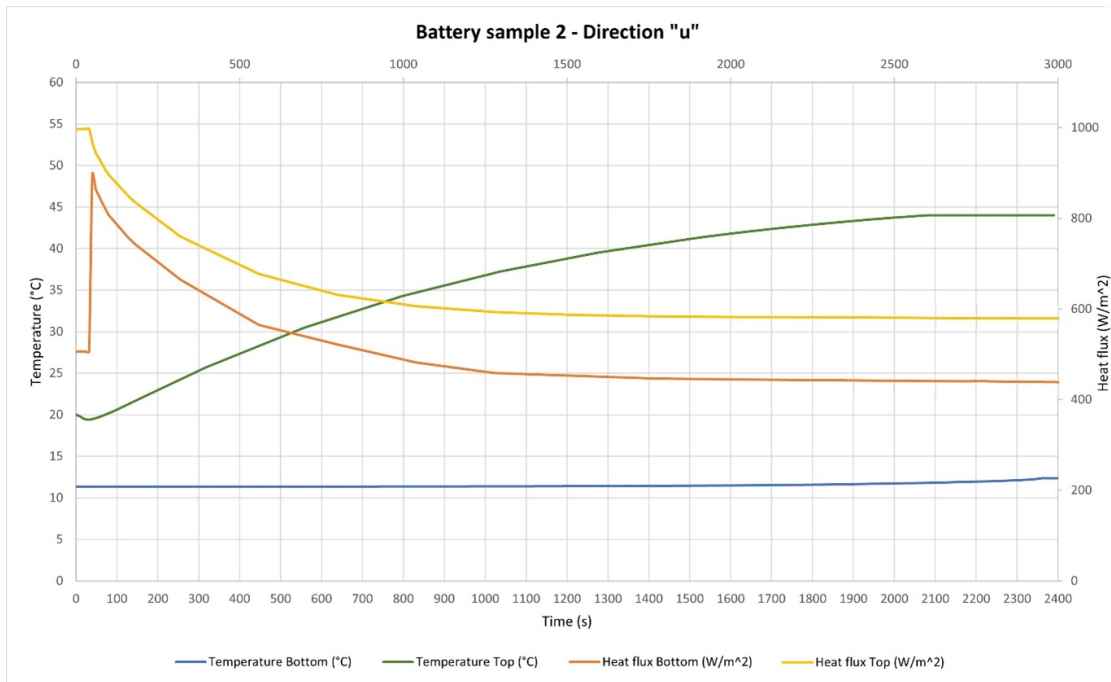


Figure 4.26: Simulated plots relative to sample 2 in "u" direction

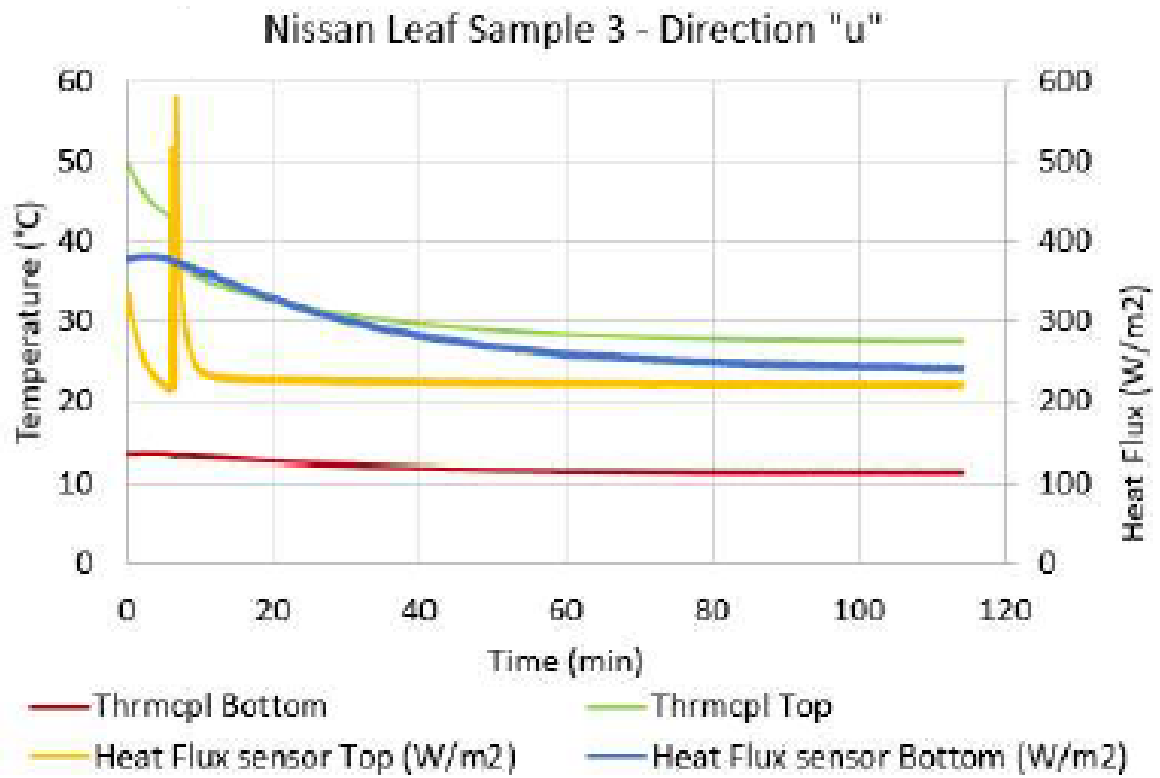


Figure 4.27: Experimental plots relative to sample 3 in "u" direction [15]

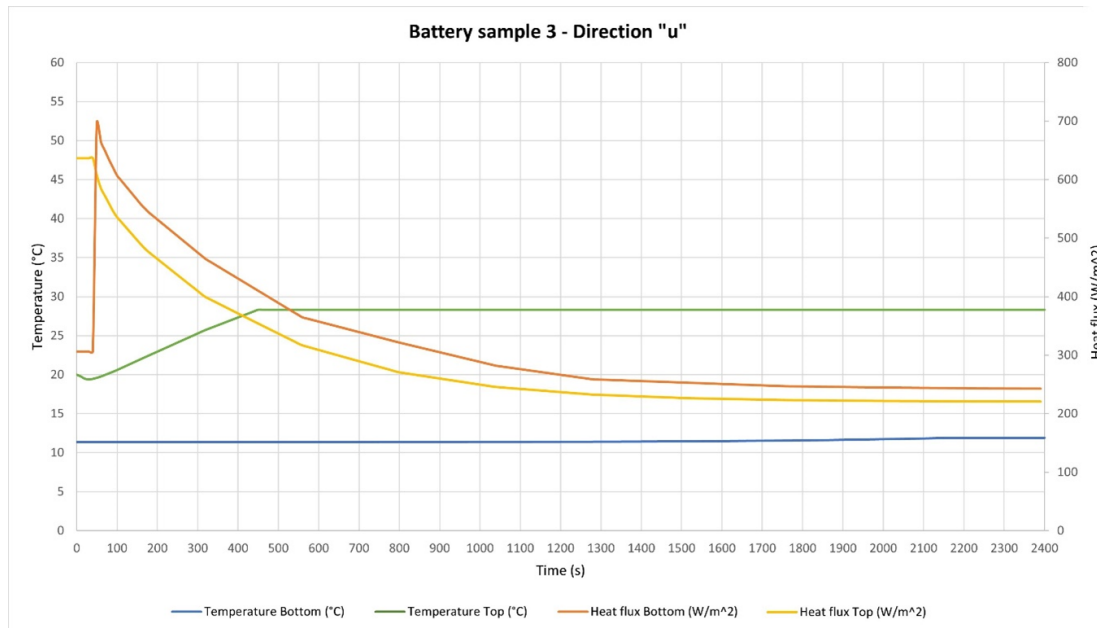


Figure 4.28: Simulated plots relative to sample 3 in "u" direction

As can be seen from the graphs and the tables above, in all three directions, once the transient is extinguished, both the temperatures and the heat-fluxes of the simulation and the experiment have pretty much the same trend. For the simulation, the "through-plane" thermal conductivity is lower with respect to the "in-plane" thermal conductivity to about a factor  $\times 34$ , while in the experiment about a factor  $\times 35$ .

In the "w" direction of sample 2, it was possible to perfectly replicate the temperature difference between top and bottom with a value of  $10.49^{\circ}\text{C}$  instead of  $10.37^{\circ}\text{C}$ . In contrast, for sample 3, it was not possible, under the same conditions, to recreate the same difference of temperature therefore instead of having a delta of  $9.52^{\circ}\text{C}$  there is a temperature gradient of  $8.6^{\circ}\text{C}$ . This is because it was not possible to simulate the heatsink in the model due to the limitations of the computer's RAM.

Furthermore, it must be taken into consideration that the measurements taken in the laboratory have an uncertainty due to the various devices, and the value of the uncertainty related to the two thermal conductivities calculated is approximately 24%.

Regarding the measurements in the "v" and "u" directions, also, in this

case, it is necessary to consider that for the laboratory values, there is an uncertainty that belongs to a range of 10-17% and that not in all four cases it was possible to replicate the perfect value of the  $\Delta T$ .

Moreover, another source of errors from the simulation point of view is caused by the adopted single-layer approach. Taking into account the paper "*Investigation of 3D multi-layer approach in predicting the thermal behavior of 20Ah Li-ion cells*"[16], it is possible to see thermal behavior of the single-layer and multi-layer cell approaches are compared with experimental results. The results show that the error of estimates is halved if the multi-layer approach is applied. Hence, the results showed that the multi-layer cell approach represents the thermal behavior of the Li-ion cell more accurately.

The multi-layer cells consist of repeating units of the positive current collector, positive electrode, separator, negative electrode, and negative current collector. If the thickness of the cells is kept constant, the number of layers is used as the controlling parameters. As the number of layers increases, the thickness of each layer decreases. Consequently, the total amount of active material remains the same in all the developed cells.

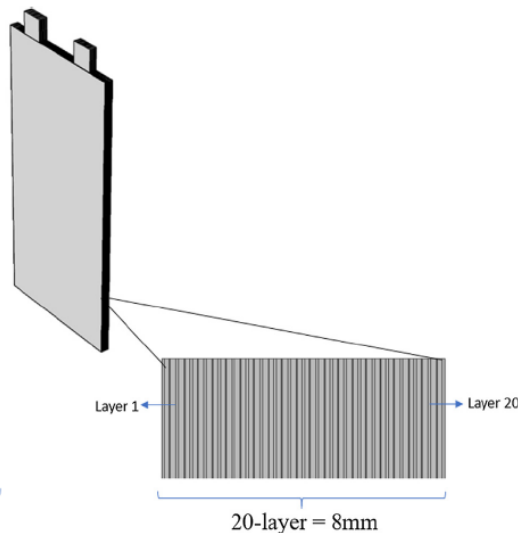


Figure 4.29: 3D Multilayer cell [16]

## 4.2 Modelling and simulation of a device to determine the influence of pretension force on the heat-flux sensor

This section shows the concept of the creation (method, modeling, and simulation) of a device capable of supporting experiments for different pretension force and temperature gradient values to answer the research question expressed in the 1 chapter.

Since in the experiment the used heat-flux sensor is the *FHF02* model produced by the company “*Hukseflux Thermal Sensors*”, the device is modeled to fit the sensor.

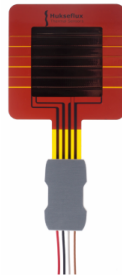


Figure 4.30: FHF02 sensor [12]

FHF02 is a standard model for general-purpose heat flux measurement. It has an integrated temperature sensor and thermal spreaders to reduce thermal conductivity dependence. It measures heat flux through the object in which it is incorporated or on which it is mounted, in  $W/m^2$ . The sensor is a thermopile. Moreover, a type T thermocouple is integrated.

A thermal spreader, a conductive layer covering the sensor, helps reduce the thermal conductivity dependence of the measurement. In addition, the passive guard area around the sensor reduces edge effects and is used for mounting.

The heat flux in  $W/m^2$  is calculated by dividing the sensor’s output, a small voltage, by sensitivity. The manufacture provides the sensitivity. More information about the theory of the heat flux sensor is already explained in the chapter 3.

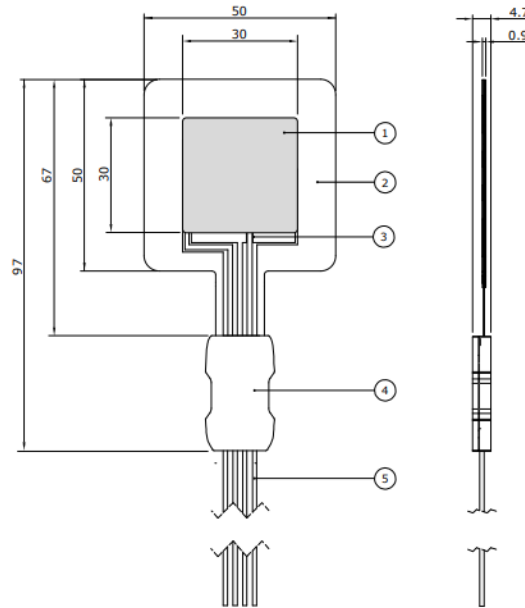


Figure 4.31: Schematic FHF02 sensor [12]

From the datasheet the data needed for the computation are:

<b>Measurement range</b>	$(-10 \text{ to } +10) \times 10^3 \text{ W/m}^2$
<b>Sensitivity range</b>	$(4 \text{ to } 8) \times 10^{-6} \text{ V}/(\text{W/m}^2)$
<b>Sensitivity (nominal)</b>	$5.5 \times 10^{-6} \text{ V}/\text{W/m}^2$
<b>Temperature sensor</b>	type T thermocouple
<b>Sensor length and width</b>	$(50 \times 50) \times 10^{-3} \text{ m}$
<b>Sensing area length and width</b>	$(30 \times 30) \times 10^{-3} \text{ m}$
<b>Sensing area</b>	$9 \times 10^{-4} \text{ m}^2$
<b>Sensor thickness</b>	$0.9 \times 10^{-3} \text{ m}$
<b>Sensor thermal conductivity</b>	$0.29 \text{ W}/(\text{mK})$
<b>Operating temperature range</b>	$-40 \text{ to } +150^\circ\text{C}$

Table 4.5: FHF02 Specifications [12]

### 4.2.1 Method

This section shows a possible method to analyze the heat flux sensor behavior during experiments in the laboratory when different force values are applied

at different  $\Delta T$ .

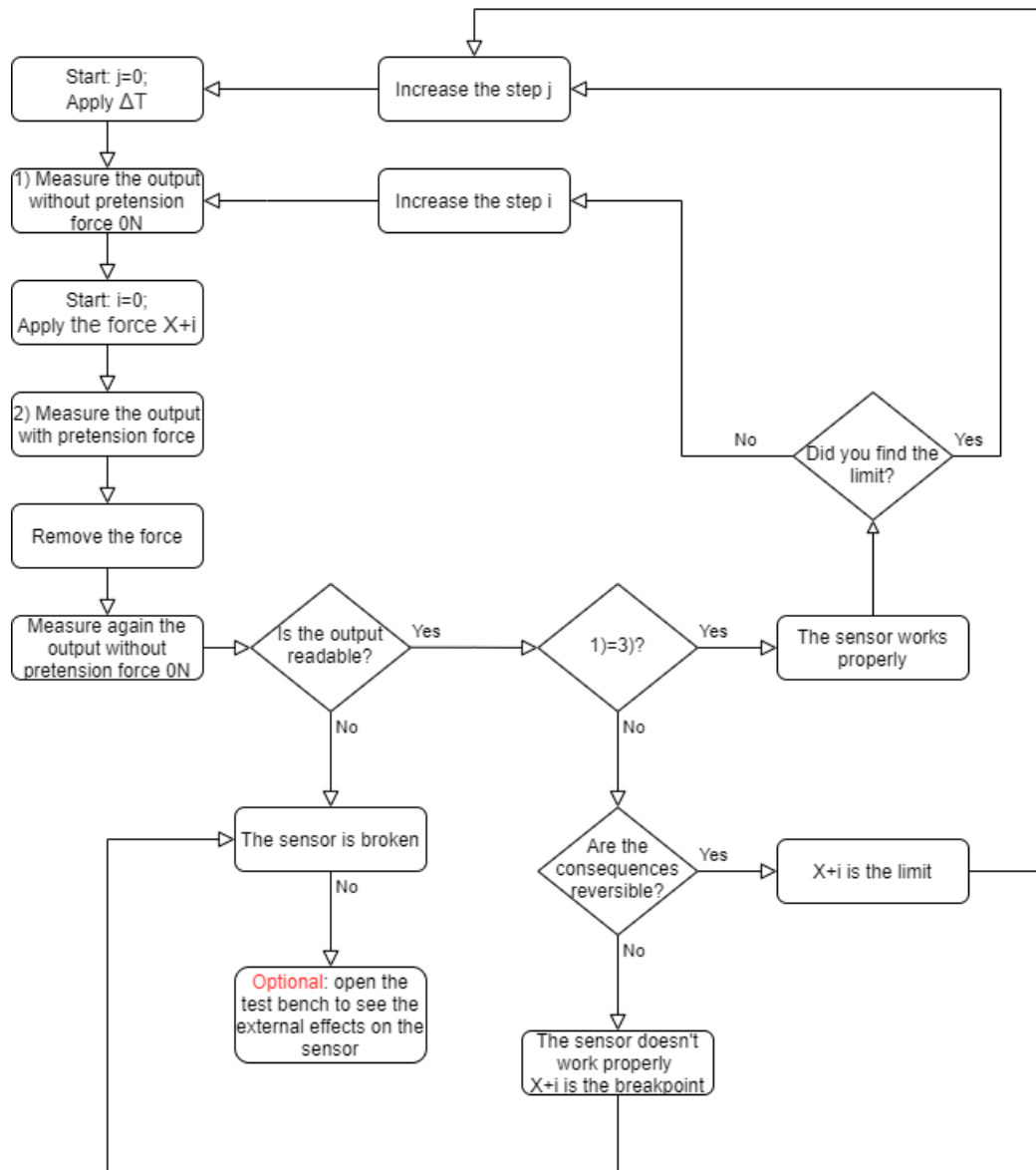


Figure 4.32: Flowchart of a possible method to study the heat flux sensor behavior

The idea is to set, at the beginning of the experiment, the force at 0N and  $\Delta T$  equal to the room temperature ( $25^{\circ}\text{C}$ ) and put the device on the structure created and explained in the previous section.

The first step is to do the calibration and measure the output of the sensor. After that, with an iterative variable "i" increase the applied force "X+i" (X is the value of pretension force belongs to the range [0,20k]N) and measure the output of the sensor. Then, remove the force and measure the output again without pretension force (0N).

Then, check that the output sensor is readable; if it isn't, this means that the sensor is broken and "X+i" is the breakpoint (**BP**), if it is the next step is to compare the two outputs and analyze if they are the same or not. Also, in this case, you can have two possibilities: they could be the same or not and understand if the consequences are reversible or not. Hence, if the values are different, and that unknown shows that the consequences are irreversible, the sensor doesn't work correctly, and "X+i" is the breakpoint, otherwise if the consequences are reversible, "X+i" is the limit **L**, which means it is the last working point before reaching the breakpoint. This value is the crucial point of the whole thesis; in fact, it allows you to understand until the heat flux sensor can stand a specific value of force.

$$BP = L + \epsilon \quad (4.3)$$

Find a limit value for the force at a specific temperature condition does not imply that the limit is always the same for all the temperatures that belong to the range of the operating temperature of the lithium-ion battery; for this reason, another iterative variable "j" is introduced. Indeed, after the value L is found, the experiment is repeated with a new value of temperature " $\Delta T + j$ " and study the sensor behavior again.

### 4.2.2 Experiment design

Since the intent is to recreate the effects of breathing and swelling on the lithium-ion battery, it is possible to use a device that recreates these effects by applying an external force on the test bench. To understand if the created structure is suitable for this type of experiment, this paragraph shows the mechanical and thermal study, which has been done on it, from a simulative point of view.

In the laboratory of the VSI institute, there is a device called "Robin" able to apply different values of force, and it is calibrated to have a range [0,20k]N; hence the maximum applied force considered for the modeled device is 20kN.

Even if the operating temperature range of the sensor is  $[-40,150]^{\circ}\text{C}$ , the experiment will not start at  $-40^{\circ}\text{C}$  but at least at  $15^{\circ}\text{C}$  due to the work limits of the Li-ion battery cell (for more detail see the paragraph 2.1). Finally, the measurement range of the heat-flux sensor is  $(-10 \text{ to } +10) \times 10^3 \text{ W/m}^2$ . Therefore, the device was modeled, taking these parameters into consideration.

The structure is made of:

1. One holed aluminum block 50 mm x 50 mm x 15 mm;
2. Two cartridge heaters with length = 40 mm and diameter = 6.5 mm;
3. One temperature sensor probe with length = 25 mm and diameter = 1.6 mm;
4. one heat flux sensor FHF02;
5. One aluminum block 80 mm x 80 mm x 15 mm;
6. Two aluminum supporters 80 mm x 36 mm x 9 mm;
7. One heatsink 50 mm x 50 mm x 25 mm;
8. One thermal insulation foam 50 mm x 50 mm x 3 mm;
9. Two Peltier cells 40 mm x 40 mm;
10. Five digital temperature sensors DS18B20;
11. One borosilicate glass 50 mm x 50 mm x 10 mm for the calibration;
12. EPS box (*Expanded polystyrene*) to avoid heat source exchanges heat with the environment. The base is 80 mm x 80 mm with a hole in the center of 50 mm x 50 mm, thickness = 12 mm, height = 25.9 mm (15.9 without calibration).

The structure was designed in order to stand the external force and a varying gradient temperature.

Each element was modeled with SolidWorks, while the simulations were performed with COMSOL Multiphysics.

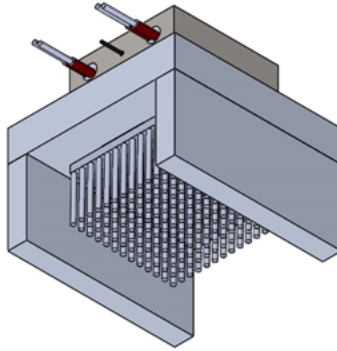


Figure 4.33: Complete structure

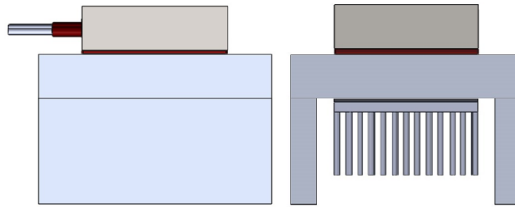


Figure 4.34: Complete structure from different views

### 4.2.3 Heating Source

To generate a heat source on top of the structure with a homogeneous temperature, two cartridge heaters and a temperature sensor (probe) are modeled and inserted inside an aluminum block with dimension of 50 mm x 50 mm x 15 mm. The three holes are equidistant between each other and are made following tolerance ISO H7/g6 [37]:

- Cartridge hole diameter  $\Phi = 6.5 \text{ mm} \rightarrow$  tolerance mm 6/10 = 0/+ 0.015;
- Temperature sensor hole diameter  $\Phi = 1.6 \text{ mm} \rightarrow$  tolerance mm 1/3 = 0/+ 0.009;
- Cartridge length hole 45 mm without tip;
- Temperature sensor length hole 25 mm without tip;
- Cartridge position completely inside the block with position from 5 mm to 45 mm;

- Temperature sensor position from 0 mm to 25 mm.

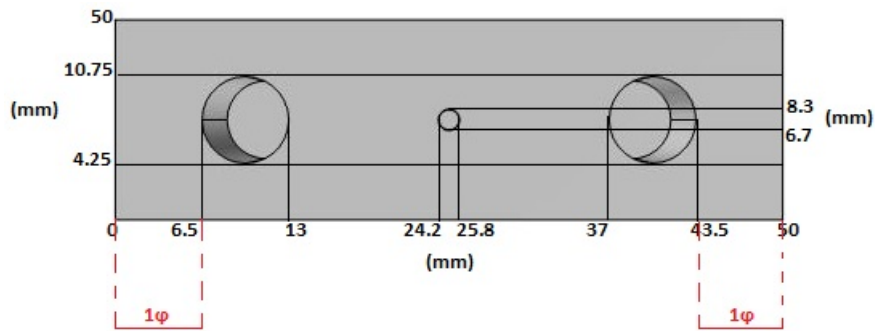


Figure 4.35: Aluminum block of the upper part and holes dimensions

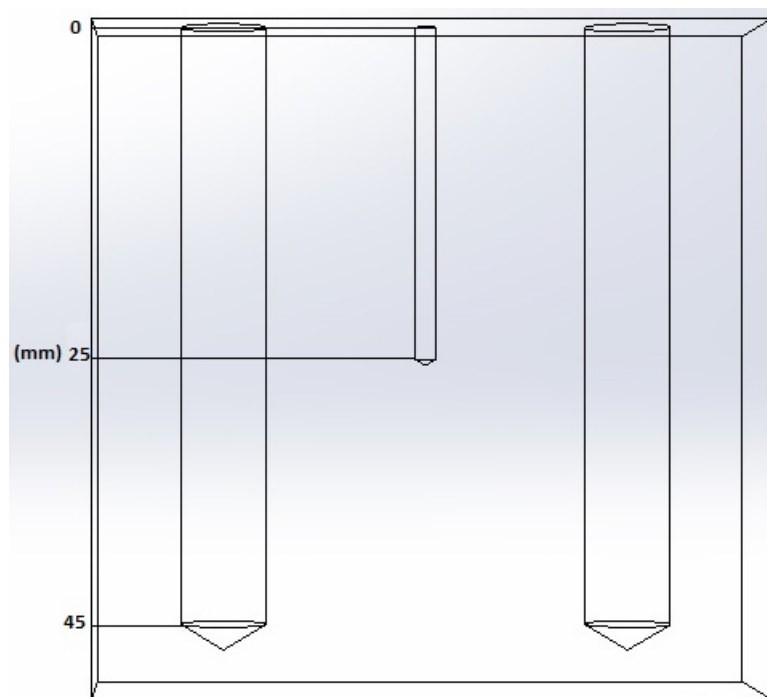


Figure 4.36: Aluminum block of the upper part and holes dimensions (top view)

For future creation in the laboratory, making the holes with a drill bit for stainless steel is advisable.

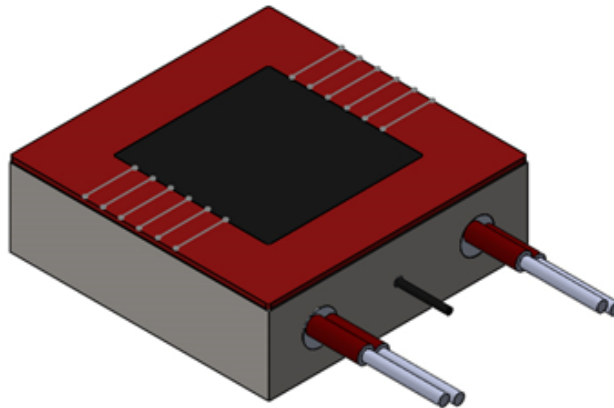


Figure 4.37: Complete model of heat source with heat flux sensor

For the modeling of the cartridge heater and the temperature probe for the simulations, reference was made to the site "*RS Components*"[38].

For the length of the probe, a greater value was chosen to reach the center of the aluminum block to have a measurement as uniform as possible.

Regarding the cartridge heater at the design stage, it is important to provide the largest number of cartridge heaters to obtain a more uniform heat distribution and reduce the power density of each heater. The distance between the heaters should respect the following values:

- 1.5 times the cartridge diameter;
- 1.0 times the cartridge diameter towards the side of the mass to be heated;
- the power density and working temperature, are the two most critical factors that affect the life of the element; to obtain greater thermal conduction for the benefit of heater, it is necessary to drill holes with minimum tolerances (it is recommended in ISO H7) and a good degree of finishing (hole without grooves and scratches);
- the cartridge for the entire length must be inserted inside the housing hole;
- to measure the temperature of the heated object, place the thermocouple equidistant from the heaters.

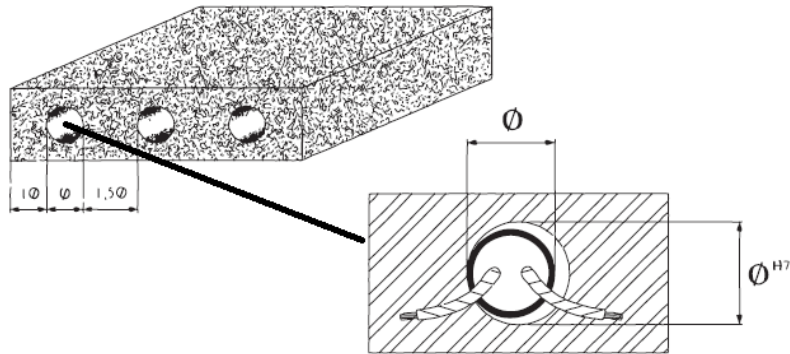


Figure 4.38: heat source front view [19]

#### 4.2.4 Cooling device

The cooling device consists of an aluminum block with dimensions of 80 mm x 80 mm x 15 mm, two Peltier cells 40 mm x 40 mm (same model of the previous section 4.12), one heatsink (reference: [39]), five digital temperature sensors (DS18B20 the same used in the experiment) in order to measure the temperature of the bottom part, and finally between the aluminum block and the heat sink is applied a thermal insulation foam 50 mm x 50 mm x 3 mm to avoid the direct connection between them.

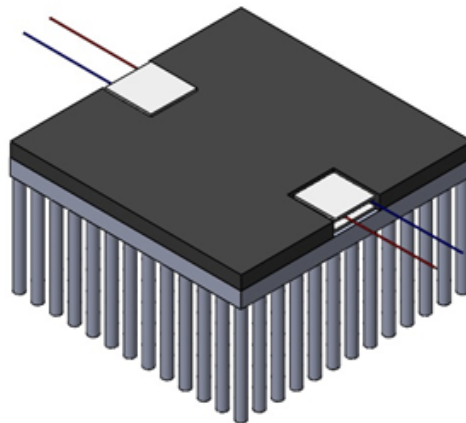


Figure 4.39: Complete model of cooling device

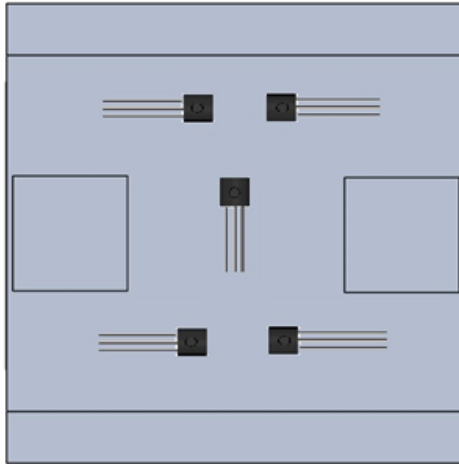


Figure 4.40: Cooling device (top view)

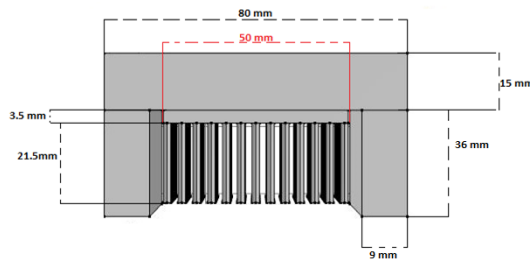


Figure 4.41: Cooling device measurements

### 4.2.5 Mechanical properties of the structure

Each piece of the structure was studied mechanically, first through mathematical equations and then at a simulation level.

#### Upper part

Regarding the mathematical equations, the following assumptions are made:

1. maximum force is applied  $F_{load} = 20\text{kN}$ ;
2. the aluminum block is considered without holes.

The following equations give the values of the stress ( $\sigma$ ) and elongation

( $\delta$ ) in the applied force direction.

$$\sigma = \frac{F_{load}}{A_{block}} = 8 \frac{N}{mm^2} \quad (4.4)$$

From Hooke's law:

$$\sigma = E\epsilon \quad (4.5)$$

Young's Elastic Modulus for aluminum  $E = 70000 \frac{N}{mm^2}$

$$\epsilon = \frac{\sigma}{E} = \frac{\delta}{t} \rightarrow \delta = \frac{\sigma}{E}t = 1.71 \mu m \quad (4.6)$$

- Area of the block  $A_{block} = 2500 \text{ mm}^2$
- thickness of the block  $t = 15 \text{ mm}$

From the computation at 20kN the elongation  $\delta$  of a not holed aluminum block is  $1.71 \mu m$  and it is negligible since the tolerance range of the holes is  $[9,15] \mu m$ .

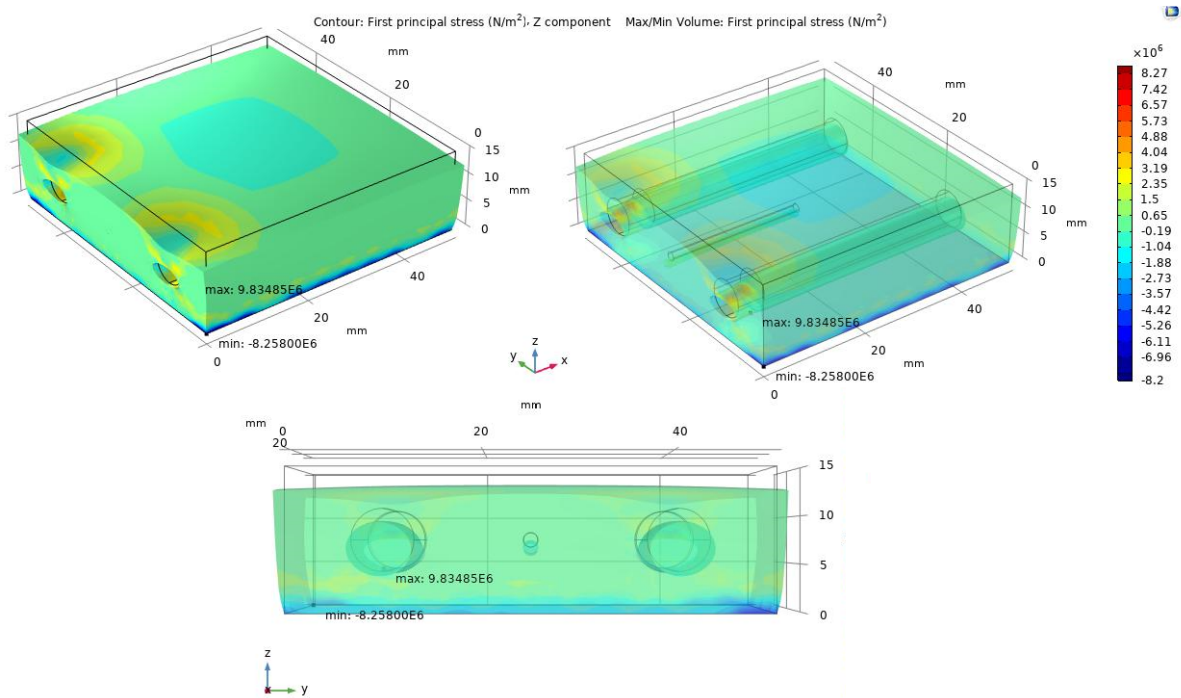


Figure 4.42: Mechanical study of heat source (stress)

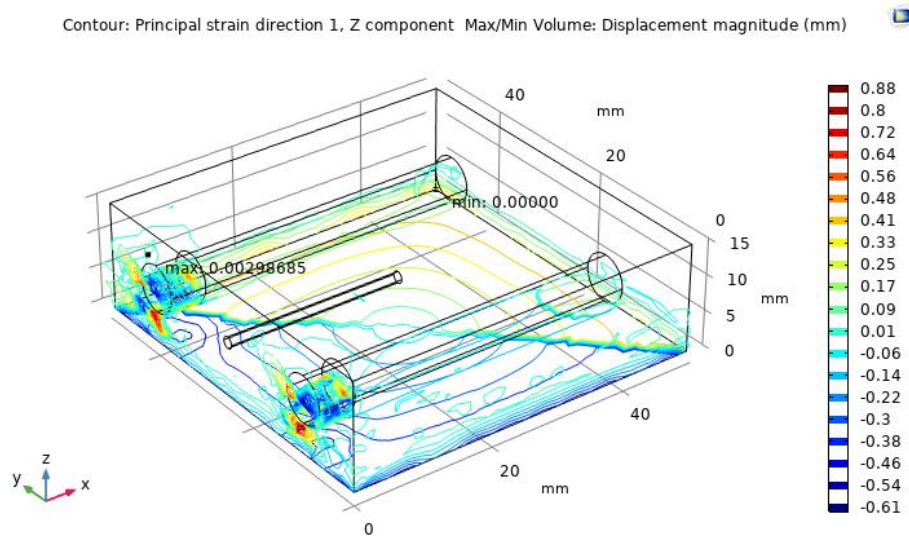


Figure 4.43: Mechanical study of heat source (elongation)

From the computation, the stress is about  $8 \text{ N/mm}^2$  and the elongation  $1.71 \mu\text{m}$ ; instead of from the simulation, the values are slightly different; in fact, the stress is about  $9.8 \text{ N/mm}^2$  and the elongation  $2.9 \mu\text{m}$ . Also, the elongation is negligible since it doesn't belong to the tolerance range of the holes. However, the difference between the values is that a solid block without holes was considered in the simplification calculations and the excessive simplifications assumed in the initial hypotheses.

### Lower part

A similar speech was made for the lower part of the structure. Regarding the mathematical equations, the following assumptions are made:

1. maximum force is applied  $F_{load} = 20\text{kN}$ ;
2. Area of the plate 1:  $80 \text{ mm} \times 80 \text{ mm}$ ;
3. thickness of the plate 1:  $15 \text{ mm}$ ;
4. the heating source is centered in the middle of the plate 1;
5. the force is concentrated in the structure;
6. symmetrical structure; height of the supports 2-3:  $h = 28 \text{ mm}$ , in this way the heatsink is  $3 \text{ mm}$  from the ground;

7. length of the supports 2-3:  $L = 80 \text{ mm}$ ;
8. Ultimate Tensile Strength (UTS)  $\in [70,180] \text{ N/mm}^2 \rightarrow$  consider the average of UTS:  $\sigma_B = 125 \text{ N/mm}^2$ ;
9. Neglect the weight of the heat source since  $\ll F_{load}$ ;
10. safety factor  $n = 6$ .

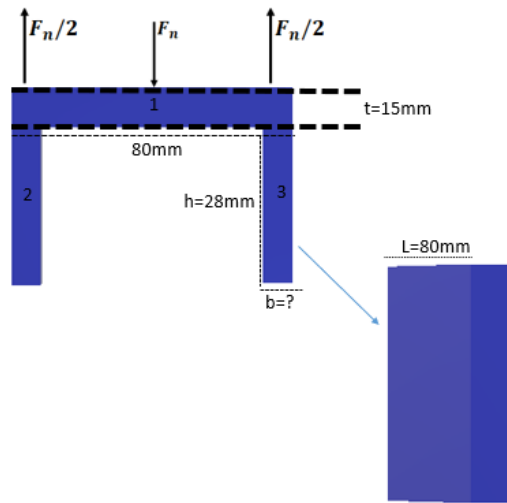


Figure 4.44: Schematic of the lower part (1)

To calculate the supports base  $b$ :

$$\sigma_W = \frac{\sigma_B}{n} = 20.8 \frac{N}{mm^2} \quad (4.7)$$

$$\sigma = \frac{F_{load}}{A_{support}} \rightarrow A_{support} = \frac{F_{load}}{\sigma_W} = 961.5 mm^2 \quad (4.8)$$

$$A_{support} = b \times L \rightarrow b = \frac{961.5}{80} = 12 mm \quad (4.9)$$

$\sigma_W$ : working stress

Regarding the computation of the bending on the horizontal plate (*deflection*  $f$ ):

$$f = \frac{F_{load} l^3}{48 E J} = 0.08 mm \quad (4.10)$$

$l$  is considered the distance between the centers of the two supports.

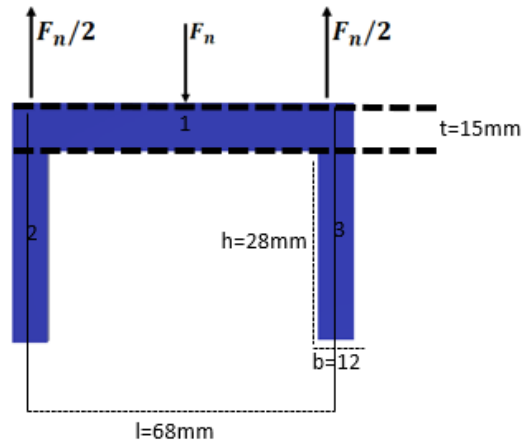


Figure 4.45: Schematic of the lower part (2)

Unfortunately, with these values of the supports going to do the simulation, the results are not good. As seen from the figure, with a load of 20kN, the structure flexes more than it should. In this way, the heatsink touches both the side supports and the ground not working well.

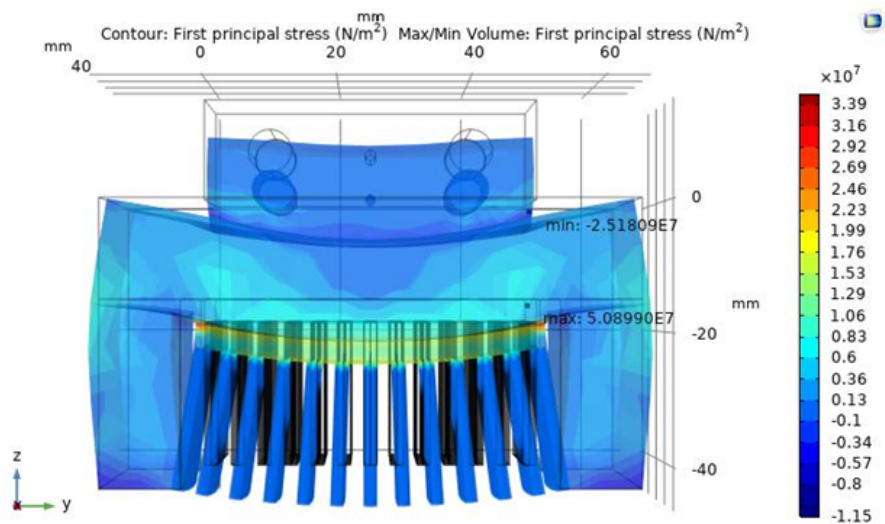


Figure 4.46: Mechanical study of cooling device (stress) with first dimensions

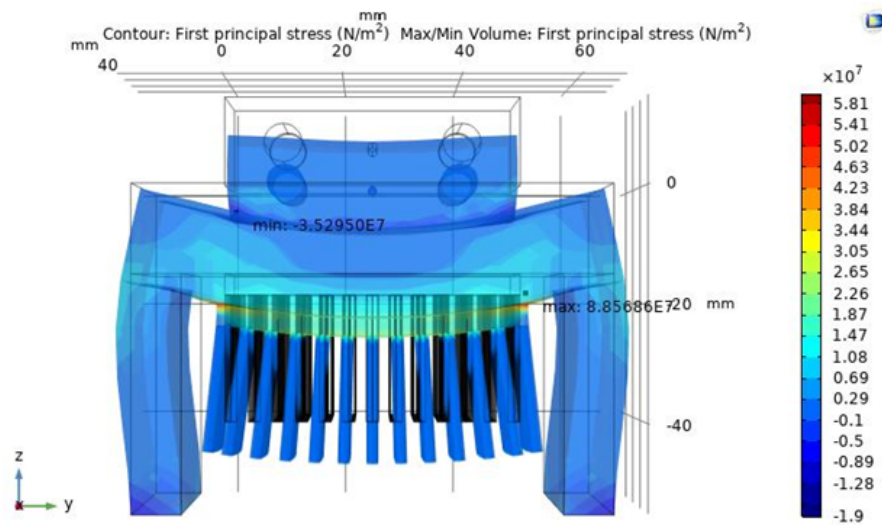


Figure 4.47: Mechanical study of cooling device with second dimensions

This implies that the values used are too approximate due, also in this case, to excessive simplifications. Therefore, with a "trial and error" procedure, in order to have a functioning structure, new supports values are obtained:

- $h = 36 \text{ mm}$ ;
- $b = 9 \text{ mm}$ ;

Now the heatsink, when the applied force is 0N, is 11 mm from the ground; instead, when the applied force is 20kN, it is 4 mm (Figure 4.47).

### 4.2.6 Energy balance

The heat transfer in the structure occurs by conduction. So, to compute the heat transfer value from top to bottom and obtain a temperature profile, calibration measurements with borosilicate glass are made. From the datasheet, at 15°C, the thermal conductivity of the borosilicate glass is 1.08 W/mK; this means that the heat source and the cooling device must create a temperature gradient of 15°C. Also, the upper block has been heated to a temperature of 150°C (maximum sensor reading value). Consequently, the other side of the glass was set at a temperature of 135°C (the sensor's part) to understand at what temperature the cooling device should be. Summarizing the values are:

- $T_{high} = 150^{\circ}\text{C}$
- $T_m = 135^{\circ}\text{C}$
- $\Delta T = 15^{\circ}\text{C}$
- thermal conductivity of the glass 1.08 W/mK
- Area of the glass 2500  $\text{mm}^2$
- thickness of the glass 10 mm
- thermal conductivity of the sensor 0.29 W/mK
- Active area of the sensor 900  $\text{mm}^2$
- thickness of the sensor 0.9 mm

From the following equation, it is also possible to compute the thermal resistances of the sensor and the glass:

$$R = \frac{t}{k \cdot A} \quad (4.11)$$

Hence, the values of the resistances are:

- $R_{glass} = 3.7 \text{ K/W}$
- $R_{sensor} = 3.45 \text{ K/W}$

From Fourier's law, the heat transfer from the heat source to the glass is 4.05 W.

Considering the equivalent electrical scheme, it is possible to notice that the two components are in series, this means that the heat transfer rates and consequently the heat fluxes are the same:

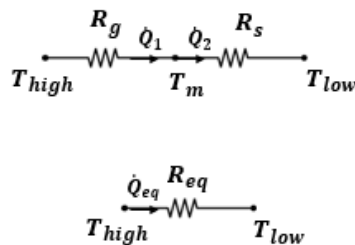


Figure 4.48: Equivalent electrical scheme

Now, it is possible to calculate  $T_{low}$ :

$$T_{low} = T_m - \frac{R_{glass}}{R_{sensor}}(T_{high} - T_m) \approx 119^\circ C \quad (4.12)$$

Where  $T_{high}$  is the temperature of the heat source,  $T_{low}$  is the temperature of the cooling device, and  $T_m$  is the temperature of borosilicate glass and sensor.

Finally is possible to obtain the heat flux:

$$\dot{q} = \frac{\dot{Q}_{eq}}{A_{glass}} = 1620 W/m^2 \quad (4.13)$$

$\dot{q}$  is in the measurement range of the heat flux sensor  $(-10 \text{ to } +10) \times 10^3 W/m^2$ .

As far as the temperature profile is concerned, making the assumption that  $T_{high}$  and  $T_{low}$  are constant and considering a homogeneous temperature distribution in the two aluminum blocks:

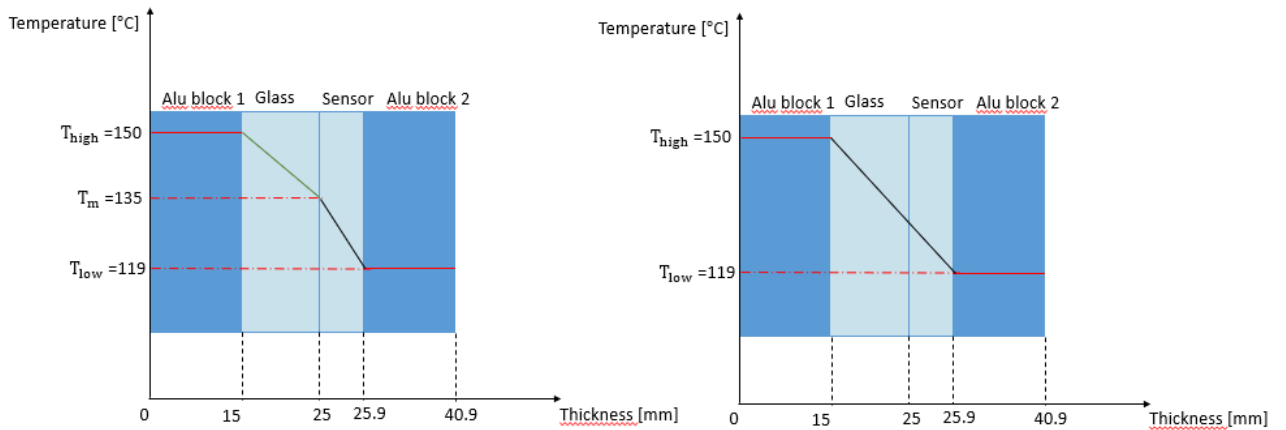


Figure 4.49: Temperature profile

As for the mechanical behavior also for the thermal one, it is possible to note that the simulation deviates from the calculated values.

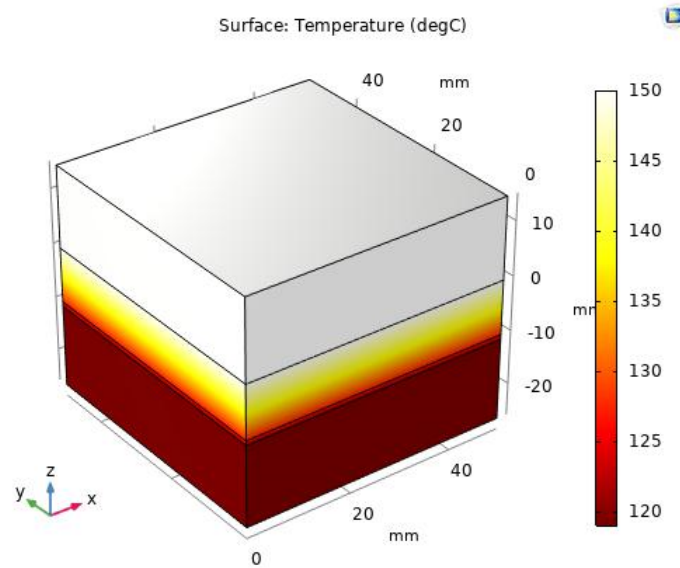


Figure 4.50: Calibration: Temperature study

The average values are:

- heat transfer rate 4.8 W
- heat flux  $1943 \text{ W/m}^2$
- $T_m = 138^\circ\text{C}$

### 4.2.7 Heat source

Once the upper aluminum block has been drilled and the cartridge heaters inserted, it remains to be understood how long the heater takes to get the block to  $150^\circ\text{C}$  and how much heat is required starting from an initial temperature of  $25^\circ\text{C}$  (room temperature).

As before, here too mathematical calculations were made first and then compared with the simulation values.

The hypotheses are:

- Initial temperature  $T_i = 25^\circ\text{C}$
- final temperature  $T_f = 150^\circ\text{C}$
- aluminum block mass  $m = 0.10 \text{ kg}$

- specific heat capacity of aluminum  $c_p = 896 \text{ J/kg}^\circ\text{C}$
- power of cartridge heater  $\dot{Q} = 30 \text{ W}$  [38]
- two cartridge heaters

The needed heat is:

$$Q = mc_p\Delta T = mc_p(T_f - T_i) = 11200J \quad (4.14)$$

The time needed for each cartridge heater is:

$$\Delta T = \frac{Q}{\dot{Q}} = 373s \approx 6min \quad (4.15)$$

Since there are two cartridge heaters, the time is half  $\approx 3 \text{ min}$ .

Regarding the simulation, figures at different times are shown until the desired temperature is reached. In this case, the time is around 3.1 minutes (Figure 4.52). As far as the needed heat is concerned, the following graph confirms the previously calculated value (Figure 4.51).

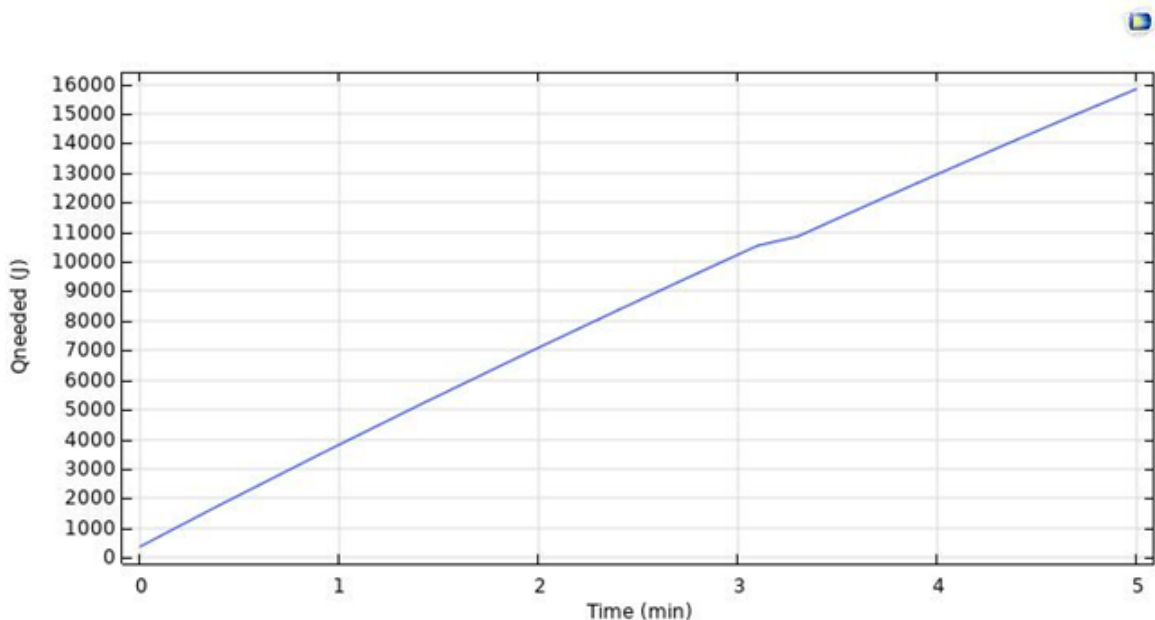


Figure 4.51:  $Q_{needed}$  from 0 to 5 min

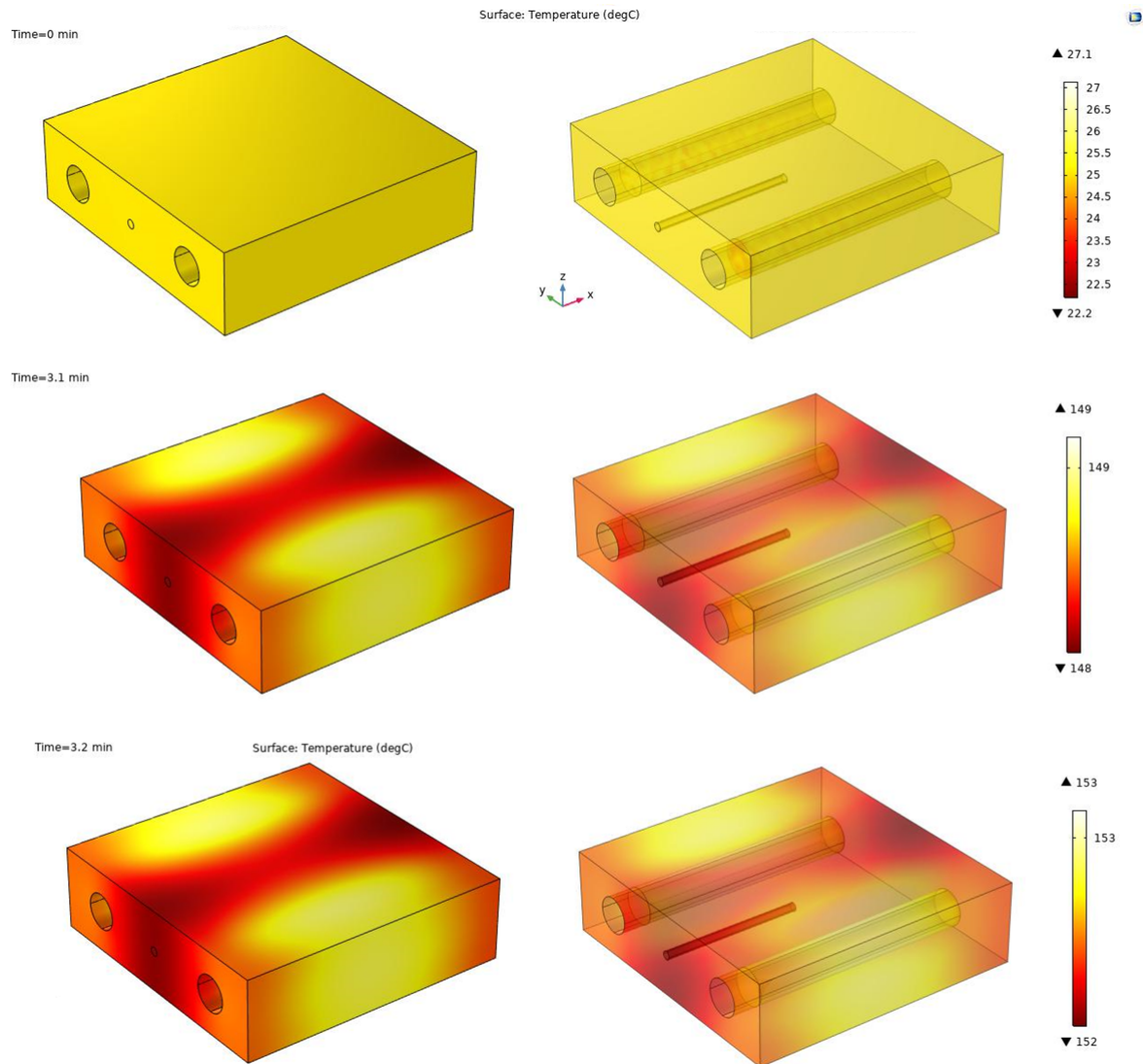


Figure 4.52: Heating at different minutes

Another aspect to consider is the heat exchanged between the heat source and the surrounding environment. This heat exchange occurs by laminar convection. Due to this phenomenon, the temperature of the aluminum block cannot remain constant, so it was decided to surround it with a thermally insulating box (EPS box) in order to make the structure adiabatic. The hypotheses are:

- $T_{env} = 25^{\circ}\text{C}$
- $T_{block} = 150^{\circ}\text{C}$

- exchange surface  $A_{ex} = 50 \text{ mm} \times 15 \text{ mm}$  (side of the block)
- usually the convective coefficient of the air is in the range  $[2.5, 25] \text{ W/m}^2\text{K}$  [40]. In this case  $h = 2.5 \text{ W/m}^2\text{K}$  is considered
- EPS thermal conductivity  $0.03 \text{ W/mK}$

Thanks to these information is possible to compute the heat loss with environment through Newton's law:

$$\dot{Q}_{loss} = h \cdot A_{ex} \cdot (T_{block} - T_{env}) = 0.23W \quad (4.16)$$

Adding an EPS box with the previous value of the heat loss, it is possible to compute the thickness that the box should have. Considering to cover only the heat source, the area of the box is equal to the exchange surface and from Fourier's law:

$$\dot{Q}_{loss} = k_{EPS} \cdot A_{EPS} \frac{T_{block} - T_{env}}{t_{EPS}} \rightarrow t_{EPS} = k_{EPS} \cdot A_{EPS} \frac{T_{block} - T_{env}}{\dot{Q}_{loss}} = 12mm \quad (4.17)$$

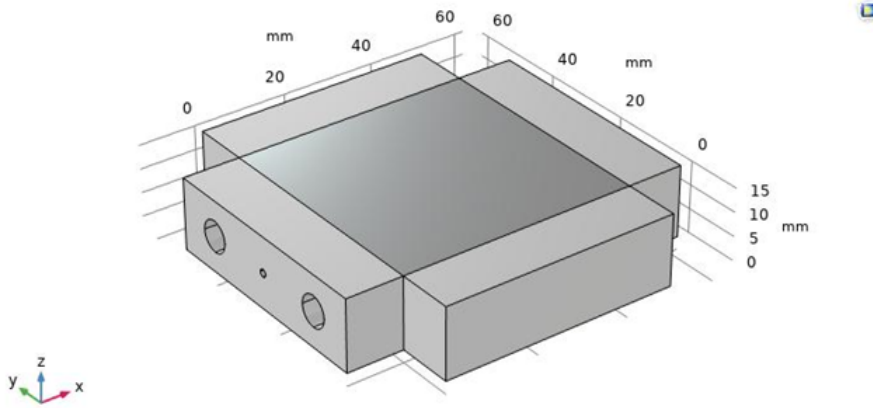


Figure 4.53: Heat source with EPS box

Doing the simulation with the EPS box, the heat source takes more time to arrive at  $150^\circ\text{C}$  (around 3.3 min), and its average temperature is  $149.32^\circ\text{C}$ .

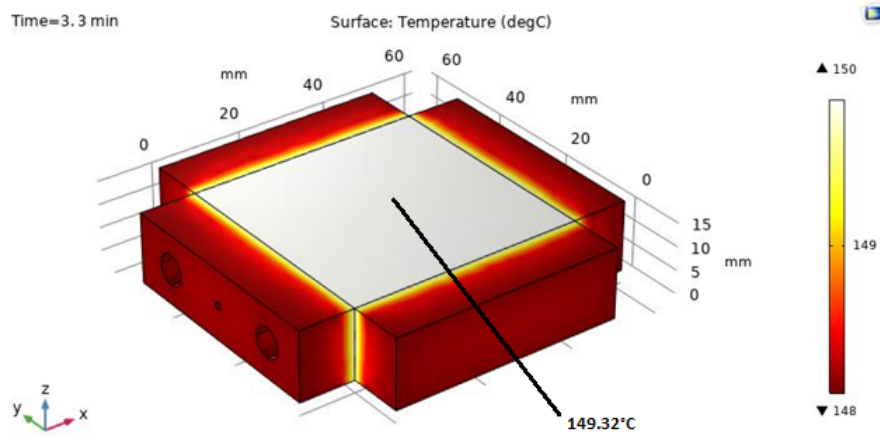


Figure 4.54: Heat source with EPS box: temperature study

From the following graph, it can be seen that at about 3.3 min, when the heat source is at almost 150°C, the heat lost is around 0.2 W, consistent with the previously calculated value.

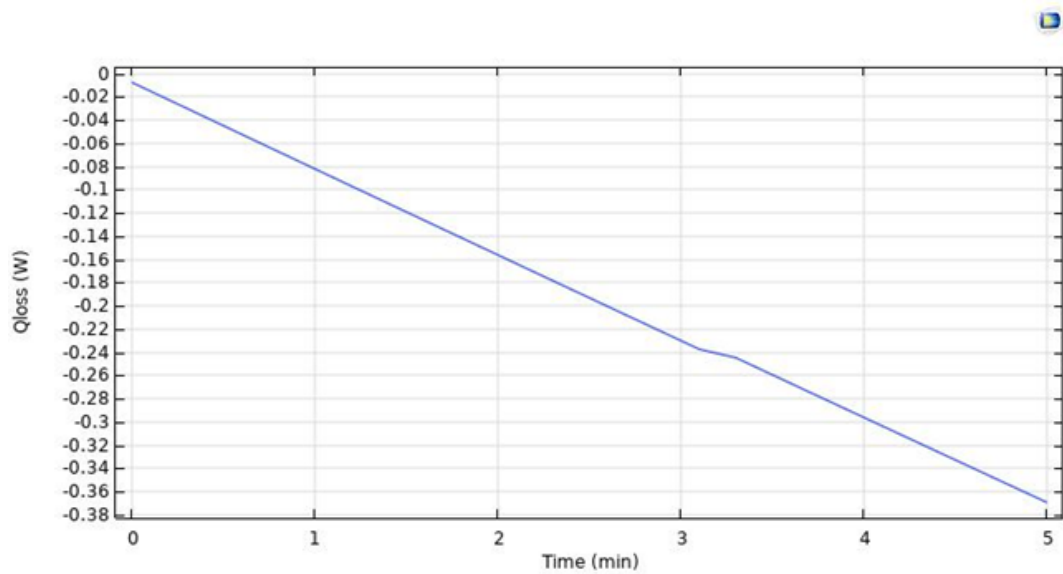


Figure 4.55:  $Q_{loss}$  with EPS box from 0 to 5 min



# Chapter 5

## Conclusion & Outlook

The present thesis wants to provide a reference text regarding the standard procedure for the simulations of the thermal behavior of the cells using the COMSOL Multiphysics software with the FEA technique. Furthermore, it also wants to provide the results of these simulations and compare them with the empirical values obtained from the experiments in order to understand how much the actual values differ from the simulated ones and how much the sources of error (simplifications, uncertainty devices) can affect a laboratory experiment. In particular, in this work, the thermal behavior was analyzed. The values of the in-plane and trough-plane thermal conductivities of a pouch cell, discharged at 1C and with an SoC equal to 30%, were analyzed.

The first part of the work was to simulate the cells to obtain information on their behavior during working conditions. Thus, it was not a simple comparison of data, but a testing process on reference cells, to obtain values that were not only taken from the literature or standard models but that reflected the actual cell analyzed in order to obtain a comparison truthful and real. Therefore, the testing phase is an integral part of the beginning and end of the work and not only used as a final comparison. From this phase, interesting insights have been obtained on the values of thermal conductivities, within particular the variations they undergo during the simulations.

However, an important aspect is not considered in the literature during the study of thermal behavior. Lithium-ion batteries being subjected to breathing and swelling mechanisms tend to change their volume, particularly in thickness direction. This geometric modification inevitably entails changing behavior for thermal parameters such as temperature distribution, heat flux,

and thermal conductivity. It is in this regard that the object of the thesis was to expand the initial idea of the experiment with an already existing device also to add mechanical modifications to simulate the mechanisms mentioned above in the battery. In this way, it is easier to understand how the change in volume affects the thermal parameters. Above all, it is possible to understand and prevent the consequences that they could have in terms of working condition, performance, and life cycle for the battery itself.

To make the current device capable of being able to withstand external loads to be applied to the battery, in this specific case a force that belongs to a range  $[0,20k]$  N, it is important to analyze all the devices involved in order to be sure that are robust enough to handle an applied load of this magnitude and output the correct value.

Therefore, it is here that the second part of this work comes into play, in which the behavior of the heat flux sensor (model FHF02) is analyzed among the various devices involved. In fact, after accurate modeling and analysis of a new structure that takes its cue from the existing one, made more robust in order to be able to support the different force values applied, the aim is to understand the behavior of the sensor and actually what is the maximum value of pretension force, applying different values of temperature difference  $\Delta T$ , which it can sustain before breaking or giving an incorrect reading of the data.

Furthermore, as this work has mainly focused on the simulation part, the next step will be to extend the modeled device for future experiments in the laboratory.

In conclusion, if applying an external mechanical load to the questions:

- how does the sensor react?
- Which is the maximum pretension value that heat flux sensor can stand?
- Changing pretension force and temperature values, is the sensor's output always the same?

A possible solution could be exposed in the 4th chapter of the thesis.

# Bibliography

- [1] Vehicle Safety Institute.  
<https://www.tugraz.at/institute/vsi/home/>.
- [2] Rouven Christen, Gerhard Rizzo, Alfred Gadola, and Max Stöck. Test method for thermal characterization of li-ion cells and verification of cooling concepts. *MDPI*, 26 January 2017.
- [3] Evgenij Barsoukov, Jee Hwan Jang, and Hosull Lee. Thermal impedance spectroscopy for li-ion batteries using heat-pulse response analysis. *Journal of Power Sources*, 109:313–320, 2002.
- [4] Hossein Maleki, Said Al Hallaj, J. Robert Selman, Ralph B. Dinwiddie, and H. Wang. The electrochemical society, find out more thermal properties of lithium-ion battery and components. *Journal of The Electrochemical Society*, 146:947–954, 1999.
- [5] Stephen J. Bazinski and Xia Wang. Experimental study on the influence of temperature and state-of-charge on the thermophysical properties of an lfp pouch cell. *Journal of Power Sources*, 293:283–291, 2015.
- [6] K.A. Murashko, A.V. Mityakov, J. Pyrhönen, V.Y. Mityakov, and S.S. Sapozhnikov. Thermal parameters determination of battery cells by local heat flux measurements. *Journal of Power Sources*, 271:48–54, 2014.
- [7] <https://letstalkscience.ca/educational-resources/stem-in-context/how-does-a-lithium-ion-battery-work>.
- [8] <https://www.dfrsolutions.com/blog/why-do-lithium-ion-batteries-swell>.
- [9] Ahmad Pesaran, Ph.D. Shriram Santhanagopalan, and Gi-Heon Kim. Addressing the impact of temperature extremes on large format li-ion batteries for vehicle applications. *30TH INTERNATIONAL BATTERY SEMINAR Ft. Lauderdale, Florida*, March 11-14, 2013.

- [10] Hossein Maleki, Hsin Wang, Wally Porter, and Jerry Hallmark. Li-ion polymer cells thermal property changes as a function of cycle-life. *Journal of Power Sources*, 263:223–230, 2014.
- [11] Zhoujian An, Li Jia, Liting Wei, and Chao Dang Qi Peng. Investigation on lithium-ion battery electrochemical and thermal characteristic based on electrochemical-thermal coupled model. *Applied Thermal Engineering*, 137:792–807, 2018.
- [12] <https://www.hukseflux.com/uploads/product-documents/FHF02-manual-v2006.pdf>.
- [13] J.J. Carr. *Sensors and Circuits*. Prentice Hall.
- [14] <https://en.wikipedia.org/wiki/Thermocouple>.
- [15] Luigi Aiello, Georgi Kovachev, Bernhard Brunnsteiner, Martin Schwa, Gregor Gstrein, Wolfgang Sinz, and Christian Ellersdorfer. In situ measurement of orthotropic thermal conductivity on commercial pouch lithium-ion batteries with thermoelectric device. *MDPI*, February 10 2020.
- [16] M. Alipour, E. Esen, and R. Kizilel. Investigation of 3-d multilayer approach in predicting the thermal behavior of 20ah li-ion cells. *Applied Thermal Engineering*, 143:620—632, 2019.
- [17] <https://www.comsol.it/model/download/766871/applications.thermoelectric-cooler.pdf>.
- [18] <https://www.comsol.it/model/download/806811/models.compmat.heating-circuit-layered.pdf>.
- [19] <https://www.lorenzoniheaters.com/resistenze-elettriche-a-cartuccia-e-microtubolari/>.
- [20] <https://batteryuniversity.com/learn/article/charging-at-high-and-low-temperatures>.
- [21] Georgi Kovachev, Hartmuth Schröttner, Gregor Gstrein, Luigi Aiello, Ilie Hanzu, H. Martin R. Wilkening, Alexander Foitzik, Michael Wellm, Wolfgang Sinz, and Christian Ellersdorfer. Analytical dissection of an automotive li-ion pouch cell. *MDPI*, October 31 2019.

## BIBLIOGRAPHY

---

- [22] Huaqiang Liu, Zhongbao Wei, Weidong He, and Jiyun Zhao. Thermal issues about li-ion batteries and recent progress in battery thermal management systems: A review. *Energy Conversion and Management*, 150:304–330, 2017.
- [23] Myounggu Park, Xiangchun Zhang, Myoungdo Chung, Gregory B. Less, and Ann Marie Sastry. A review of conduction phenomena in li-ion batteries. *Journal of Power Source*, 195:7904–7929, 2010.
- [24] Amartya Mukhopadhyay and Brian W. Sheldon. Deformation and stress in electrode materials for li-ion batteries. *Progress in Materials Science*, 195:58–116, 2014.
- [25] Keiji Takata. In-situ imaging of li intercalation in graphite particles in an li-ion battery. *Journal of Microscopy*, 266:58–116, 2014.
- [26] David L. Chandler. How some battery materials expand without cracking. *MIT News Office*, April 12, 2017.
- [27] M. Broussely, F. Bonhomme Ph. Biensan, Ph. Blanchard, S. Herreyre, K. Nechev, and R.J. Staniewicz. Main aging mechanisms in li ion batteries. *Journal of Power Sources*, 146:90–96, 2005.
- [28] Thermal runaway: Understanding the fundamentals to ensure safer batteries. *Battery Power*, September 19, 2019.
- [29] Tfull thermal characterization of large format li-pouch for better ev thermal management. *Green Car Congress*, May 30, 2017.
- [30] Thomas Grandjean, Anup Barai, Elham Hosseinzadeh, Yue Guo, Andrew McGordon, and James Marco. Large format lithium ion pouch cell full thermal characterization for improved electric vehicle thermal management. *Journal of Power Sources*, 359:215–225, 2017.
- [31] Yuan Ci Zhang, Olivier Briat, Jean-Yves Deletage, Cyril Martin, Guillaume Gager, and Jean-Michel Vinassa. Characterization of external pressure effects on lithium-ion pouch cell. *IEEE International Conference on Industrial Technology (ICIT)*, pages 2055–2059, 2018.
- [32] <https://batteryuniversity.com/article/bu-410-charging-at-high-and-low-temperatures>.

## BIBLIOGRAPHY

---

- [33] <https://www.linkedin.com/pulse/temperature-effect-lithium-ion-battery-nancy-wong>.
- [34] R. Wenige, M. Niemann, U. Heider, M. Jungnitz, and V. Hilarius. *Liquid Electrolyte Systems for Advanced Lithium Batteries*. 30 May 1998.
- [35] Matthias Fleckenstein, Sebastian Fischer, Oliver Bohlen, and Bernard Bäker. Thermal impedance spectroscopy - a method for the thermal characterization of high power battery cells. *Journal of Power Sources*, 223:259–267, 2013.
- [36] <https://docs.rs-online.com/fd64/0900766b8091add7.pdf>.
- [37] <https://www.ilcalibro.it/h7.htm>.
- [38] <https://docs.rs-online.com/393c/0900766b81584918.pdf>.
- [39] <https://docs.rs-online.com/15f0/0900766b80d52083.pdf>.
- [40] Philip Kosky, Robert Balmer, William Keat, and George Wise. *Exploring Engineering: An Introduction to Engineering and Design*. fifth edition: 2020.